Engineering Structures 335 (2025) 120304

Contents lists available at ScienceDirect

Engineering Structures

journal homepage: www.elsevier.com/locate/engstruct

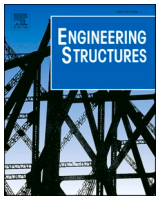

A study of combination factor of wind and snow loads on photovoltaic (PV) panels based on characterization of joint wind-snow hazard

Shan Ding, Xuanyi Zhou *

State Key Laboratory of Disaster Reduction in Civil Engineering, Tongji University, Shanghai 200092, China

ARTICLE INFO

Keywords:
Photovoltaic (PV) panel
Snowmelt model
Ground snow pressure
Wind speed
Joint hazard
Combination factor

ABSTRACT

Since the photovoltaic (PV) system uses lightweight materials, wind load and snow load are regarded as its dominant loads. However, no specific research is mentioned on the combination factor of wind and snow loads on PV panels in major international load codes [1–4]. Therefore, this paper will take the PV tracker as an example to study the combination factor of wind and snow loads on PV panels based on the characterization of joint wind-snow hazard. First, a multi-layer snowmelt model is used to obtain ground snow pressure over the years in representative cities. Then several probability models are selected to fit wind speed and ground snow pressure samples in different data pairs and the best probability model is determined. On this basis, the joint wind-snow hazard contours are derived. Finally, based on hazard contours, the finite element analysis is used to calculate the load effects of PV support. The results reveals that when wind and snow loads are both pressures and the load effects considered in the design are the axial force of columns and the bending moment of the main beam, the combination factor of wind and snow loads on the PV panel should be 0.7.

1. Introduction

Energy, which is essential for social development, has a crucial impact on economic development. With the advancement of technology and a growing awareness of environment, solar energy, as a readily available, safe and clean alternative, has gradually attracted more attention, leading to a booming PV industry globally. The PV system is composed of PV support and the modules on the support. Due to the light weight of the two parts, the PV system can be easily damaged under the combined action of wind and snow. Therefore, how to consider the combined effects of wind and snow loads is an important consideration in PV structural design.

Many researches have been done regarding the wind load and snow load on PV panels respectively. For wind load, Abiola-Ogedengbe et al. [5] measured the wind load on a single row of PV panels by wind tunnel test and found that the wind load in the vertical direction was symmetrically distributed along the central axis while the wind load in the oblique direction did not have this characteristic. In addition, the greater the tilt of the module, the stronger the wind load is. Reina et al. [6] used computational fluid dynamics to calculate the average wind load of the ground-mounted PV trackers array. Chu et al. [7] used wind tunnel tests to study the wind pressure distribution of PV tracker installed on flat roof buildings subjected to different wind directions, azimuth angles, inclination angles and base heights. Ma et al. [8] studied the interference effect of PV panels on the wind load by changing the inclination, wind direction and the number of PV panels in the wind tunnel, and obtained the wind pressure coefficient of the PV panel array. Li et al. [9] studied the influence of PV panel spacing, PV panel inclination and parapet height on the wind load of PV panels through wind tunnel test. Ma et al. [10] studied the wind load of single-row PV modules and PV arrays through wind tunnel tests. The results showed that the change of wind load of the first row of PV modules in the PV array with inclination was similar to that of single-row PV modules. Xu et al. [11], based on numerical simulation and wind tunnel test, discussed the influence of row spacing and ground clearance on the wind load. As for the researches on the snow load on PV panels. Grammou et al. [12] used the flume test to simulate the snow load distribution on the flat roof with PV panels and measured the wind-induced shape coefficients of PV panels and flat roof. Riley et al. [13] studied the magnitude of snow load, the change rate of snow load, the spatial distribution of snow load on PV panels and the influence of wind on snow load measurement in winter from 2021 to 2022 through the experimental platform built by Sandia National Laboratory. Frimannslund [14] studied how the snow reduction system of PV panels affects the reliability of roof structure and established the limit state function of

* Corresponding author.
E-mail address: zhouxytj@tongji.edu.cn (X. Zhou).

https://doi.org/10.1016/j.engstruct.2025.120304
Received 7 September 2024; Received in revised form 4 March 2025; Accepted 10 April 2025
Available online 18 April 2025

Nomenclature

A	The albedo of the snow surface
AIC	Akaike information criterion
c_s	Specific heat of snow ($kJkg^{-1}K^{-1}$)
c_w	Specific heat of water ($kJkg^{-1}K^{-1}$)
c_p	Heat capacity of air,1.005 $kJkg^{-3}℃^{-1}$
D_n	The maximum deviation between $F(x)$ and $F_n(x)$
$e(T_a)$	Air vapor pressure (kPa)
$e(T_s)$	Vapor pressure at the snow surface (kPa)
E_l	Latent heat flux ($kJm^{-2}hr^{-1}$)
$F(x)$	Cumulative distribution function
$F_n(x)$	Theoretical distribution function
h_s	Latent heat of sublimation,2834$kJkg^{-1}$
h_f	Latent heat of fusion, 335$kJkg^{-1}$
H_s	Sensible heat flux ($kJm^{-2}hr^{-1}$)
k	The number of parameters of the probability distribution model
$K_h(K_e)$	Heat conductivity (Wm^{-1}/K^{-1})
L_n	Net longwave radiation
L_a	Incoming longwave radiation ($kJm^{-2}hr^{-1}$)
L_t	Outgoing longwave radiation ($kJm^{-2}hr^{-1}$)
M_{out}^i	Rate of outflow of the ith snow layer (mhr^{-1})
M_{max}	Maximum bending moment of the main beam (kNm)
N	The sample size of probability statistics
P_{rain}	Rainfall (mhr^{-1})
$P()$	Exceeding probability
P_{snow}	Snowfall (mhr^{-1})
P_s	The pressure of snow above the snow layer (Nm^{-2})
P_{max}	Maximum axial force of columns
Q_c	Heat conduction through the snowpack ($kJm^{-2}hr^{-1}$)
Q_p	Heat advected by precipitation ($kJm^{-2}hr^{-1}$)
Q_g	Ground heat flux ($kJm^{-2}hr^{-1}$)
R^2	Coefficient of determination
R_d	Dry gas constant,0.287$kJkg^{-1}K^{-1}$
RSS	Residual sum of squares
s_0	Reference snow load (kPa)
s_k	Characteristic value of snow load (kPa)
s_{25}	Snow load of the 25-year return period (kPa)
$S_{w_{25}}$	Load effect caused by wind load of the 25-year return period
$S_{P,w_{25}}$	Maximum axial force of columns caused by wind load of the 25-year return period (kPa)
$S_{M,w_{25}}$	Maximum bending moment of the main beam caused by wind load of the 25-year return period (kNm)
$S_{s_{25}}$	Load effect caused by snow load of the 25-year return period
$S_{P,s_{25}}$	Maximum axial force of columns caused by snow load of the 25-year return period (kPa)
$S_{M,s_{25}}$	Maximum bending moment of the main beam caused by snow load of the 25-year return period (kNm)
S_m	Maximum value of combined wind and snow load effects
$S_{P,m}$	Maximum P_{max} caused by the combination of wind and snow loads (kPa)
$S_{M,m}$	Maximum M_{max} caused by the combination of wind and snow loads (kNm)
$S_{i,T}$	Load effects of live loads at T-year return period
S_n	Shortwave radiation ($kJm^{-2}hr^{-1}$)
S_0	Potential solar radiation ($kJm^{-2}hr^{-1}$)
t	Physical time (hr)
T	Return period
T_a	Air temperature (℃)
T_s	Snow surface temperature (℃)
T_g	the ground temperature under the snowpack (℃)
T_{max}	Maximum torque of the main beam (kNm)
U^i	The internal energy in snow layer i (KJm^{-2})
V,S	Random variables
v,s	Threshold values
v_0	Reference wind speed (ms^{-1})
w_0	Reference wind pressure (kPa)
w_k	Characteristic value of wind load (kPa)
w_{25}	Wind load with the 25-year return period (kPa)
W^i	Snow water equivalent of the ith snow layer (m)
W^m	Snow water equivalent of the top (mth) snow layer (m)
W_e	Sublimation or evaporation from snowpack (mhr^{-1})
x_i	The ith sample value
$\hat{\hat{x}}_i$	Sample estimation value based on the theoretical distribution function
z	the height from the bottom of the snow (m)
Δz	The thickness of the layer (m)
β_z	wind vibration coefficient
ε_s	Snow surface emissivity
ε_{ac}	Cloudy sky emissivity
σ	Stefan-Boltzmann constant, $2.07 \times 10^{-7} kJm^{-2}K^{-4}hr^{-1}$
ρ_w	The density of water (kgm^{-3})
$\rho_a(\rho)$	The density of air, 1.25 kgm^{-3}
μ	Atmospheric transmissivity
μ_r	Distribution factor of snow load
μ_s	Shape factor of wind load
μ_z	Exposure factor for wind pressure
γ_i	The mass of ice per unit volume of snow (kgm^{-3})
γ_w	The mass of water per unit volume of snow (kgm^{-3})
λ	The effective snow-conduction coefficient ($Wm^{-1}K^{-1}$)
ψ	Combination factor of wind and snow loads
ψ_P	Combination factor of wind and snow loads considering axial force of columns
ψ_M	Combination factor of wind and snow loads considering the bending moment of the main beam

roof snow load.

In winter, PV panels are often subjected to wind and snow loads, so the impact of joint wind-snow hazard should be considered in the design of PV support structure. However, there are only a few articles on the joint wind-snow hazard of buildings. Wang et al. [15] used the renewal pulse process to simulate the wind load and snow load and, by combining them in the numerical simulation, constructed the joint wind-snow hazard contour corresponding to the exceedance probability in different return periods. Peng et al. [16] obtained the wind pressure coefficient on the building surface through experiments and the roof snow pressure coefficient considering the wind-induced snow effect through numerical simulation; they then used the probability density evolution method (PDEM) to evaluate the overall reliability of the structure under the wind-snow multi-hazard coupling effect in the 100-year return period. By far, no study has been done on the joint wind-snow hazard in the design of PV support structure. However, the probability of wind load and snow load occurring simultaneously at their maximum values is small. For this reason, the combination value of the two needs to be adopted, which is obtained via the load combination factor. At present, the main international load codes [1–4] have included neither studies nor literature on the combination factor of wind and snow loads on PV panels.

Given the above-mentioned, this paper will calculate the combination factor of wind load and snow load on the PV panels based on the characterization of joint wind-snow hazard. Firstly, the ground snow pressure is simulated by multi-layer snowmelt model [17–19]. Then, this paper adopts four methods to obtain different data pairs of wind speed and ground snow pressure (referred to as "data pair") for the purpose of considering the load state when these two important loads occur at the same time. A variety of probability models are used to fit wind speed and ground snow pressure samples in these four types of data pairs respectively. According to the K-S test and AIC, the optimal probability model of the two is determined, and the joint wind-snow hazard contours of different return periods are further obtained. Furthermore, based on the combination value of wind speed and ground snow pressure on the joint wind-snow hazard contour of the 25-year return period, the load effect of PV support is calculated through finite element analysis. Finally, the combination factor of wind and snow loads on the PV panel is calculated based on the obtained load effect.

2. Methodology

This study adopts the snowmelt model [17–19] to calculate the ground snow pressure and obtains the data pairs by different methods. Then, several probability models are selected to fit wind speed and ground snow pressure samples in different data pairs and the best probability model is determined, based on which the joint wind-snow hazard contours of different return periods are calculated. Finally, finite element analysis is used to calculate the load effects of wind and snow loads of the 25-year return period, and their combined effects of the PV support for the calculation of the combination factor of wind and snow loads on the PV panel. The calculation process is shown in Fig. 1.

2.1. Multi-layer snowmelt model

According to national codes [1–4], the snow load on the building structure is calculated based on the ground snow pressure in a certain return period. Therefore, the acquisition of ground snow pressure samples is the prerequisite of this study. However, the weather station can only obtain the data of snow depth, and the amount of data is too limited to support the study. In order to obtain the ground snow pressure samples, this paper simulates the whole process of ground snow accumulation and melting based on precipitation, temperature, wind speed, relative humidity and other meteorological data through the multi-layer snowmelt model [17–19], as shown in Fig. 2.

2.1.1. Energy balance equation

The internal driving force of the snow melting process comes from the input and output of energy [20]. The energy balance equation of layer i at time t is as follows:

$$\frac{dU^i(t)}{dt} = L_n(t) + S_n(t) + H_s(t) + E_l(t) + Q_c(t) + Q_p(t) + Q_g(t) \quad (1)$$

where the calculation method of net longwave radiation L_n, shortwave radiation S_n, sensible heat H_s, latent heat E_l, the energy transferred between adjacent snow layers Q_c and energy brought by precipitation Q_p can be seen in Table 1. The ground heat flux Q_g merely affects the first snow layer at the bottom of the snowpack and is minimal [44,45]. In particular, the calculation of ground heat flux is not provided in the table but is replaced by adopting the specified constant boundary temperature. Bartelt et al. [21] hold that the soil temperature fluctuates around 0℃; Ohara and Kavvas [22] also believe that the temperature of snow near the ground is 0℃ in the case of thick snow layers. Thus, the soil boundary temperature is assumed to be 0℃.

2.1.2. Mass balance equation

The mass balance equation can describe the effects of snowfall, rainfall, snow melting, snow sublimation or evaporation on the quality of the snow layer. Compared with the snow particles and water in the snow layer, the phase change and diffusion of water vapour have less impact on the change of snow layer mass, so the influence on the mass balance equation is ignored in this paper [27]. The mass balance equation of the top layer of snow (layer m) at time t is shown in Eq. (8) in

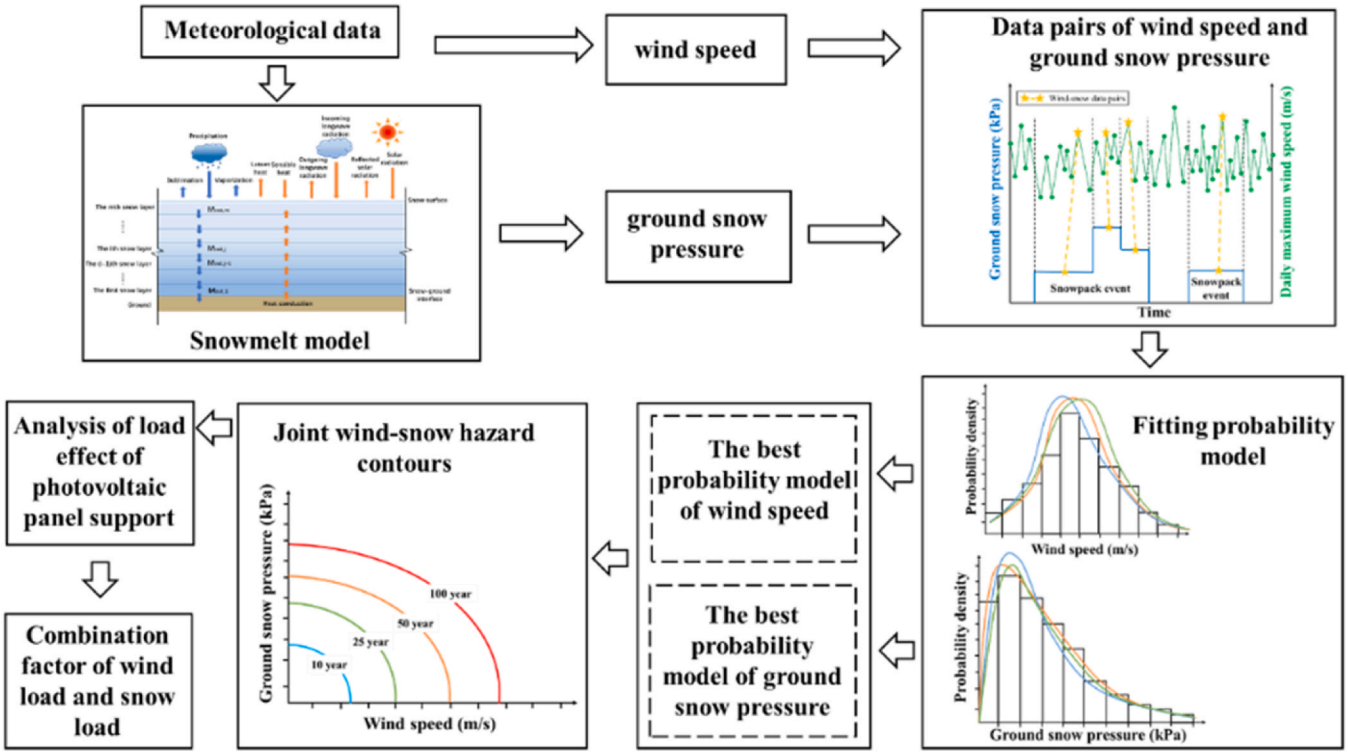

Fig. 1. Procedure of calculation of combination factor in this study.

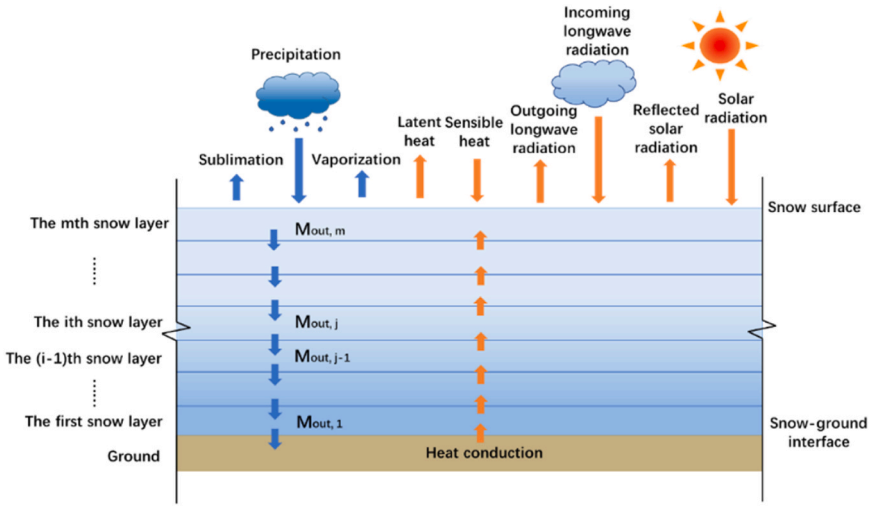

Fig. 2. Energy and mass fluxes involved in snowpack melting.

Table 1
Formula of energy calculation [17–19].

Energy	Formula	
Net longwave radiation [23]	$L_n = L_a - L_t = \varepsilon_{ac}\sigma(T_a + 273.15)^4 - \varepsilon_s\sigma(T_s + 273.15)^4$	(2)
Shortwave radiation [23]	$S_n = (1 - A)\mu S_0$	(3)
Sensible heat [24]	$H_s = \rho_a c_p K_h (T_a - T_s)$	(4)
Latent heat [25]	$E_l = K_e \frac{0.622 h_s}{R_d(T_a + 273.15)}[e(T_a) - e(T_s)]$	(5)
Heat conduction [26]	$Q_c = \lambda \frac{\partial T}{\partial z}$	(6)
Heat from precipitation [25]	$Q_P = P_{snow} c_s \rho_w \min(T_a, 0°C) + P_{rain}\left[h_f \rho_w + c_w \rho_w \max(T_a, 0°C)\right]$	(7)

Table 2. The mass balance equation of the inside and bottom layer ($1 \le i \le m - 1$) at time t is shown in Table 2, Eq. (9).

Precipitation occurs in the form of snow or rainfall. In this paper, precipitation is divided into snowfall $P_{snow}(t)$ and rainfall $P_{rain}(t)$ according to air temperature. When the air temperature T_a is lower than −1℃, all precipitation is snow; when the air temperature$T_a$is higher than 3℃, all precipitation is rainfall; when the air temperature$T_a$is between −1℃ and 3℃, the snowfall and rainfall are linearly interpolated [17,18,28]. See Eq. (10) in Table 2 for the calculation method. Latent heat can change the liquid water phase state of the snow layer. According to Dewalle et al. [29], the sublimation or evaporation of snow can be calculated according to Eq. (11) in Table 2. The calculation of outflow$M_{out}(t)$is related to the maximum water holding capacity of snow. When the liquid water content inside the snow layer exceeds the maximum water holding capacity of the snow layer, the excess liquid water will flow out of the snow layer. According to Ref. [30], the formula for calculating the maximum water holding capacity of the snow layer is shown in Table 2, Eq. (12).

2.1.3. Snowpack compaction and density

The compaction process of snow involves two stages: the destructive metamorphism stage of fresh snow and the densification process of accumulated snowpack under its gravity or the pressure of upper layers [17–19,31]. For fresh snow, because of its low density, the destructive metamorphism of the internal structure of snow is the main cause for compaction. Eq. (13) in Table 3 shows how the destructive metamorphism of the internal structure per unit thickness of the snow layer changes over time. After the destructive metamorphism stage, the compaction rate of the snow layer decreases significantly. At this point, the main cause for compaction is the gravity compaction of the snowpack. The calculation method is shown in Eq. (14) in Table 3. The total compaction rate of the snow layer is the sum of the compaction rates of the above two stages, and the calculation formula is shown in Eq. (15) in Table 3. The density of the snow layer increases with the compaction, and the calculation formula is shown in Eq. (16) in Table 3.

2.1.4. Boundary conditions

The boundary conditions between the snow surface and the snow

Table 2
Formula of mass balance [17–19].

	Formula	
Mass balance equation of the top snow layer	$\frac{dW^m(t)}{dt} = P_{rain}(t) + P_{snow}(t) - M_{out}(t) - W_e(t)$	(8)
Mass balance equation of the inside and bottom layer of snow	$\frac{dW^i(t)}{dt} = M^{i+1}_{out}(t) - M^i_{out}(t)$	(9)
Precipitation separation formula	$P_{rain} = \begin{cases} T_a \ge 3°C \\ -1°C < T_a < 3°C \\ T_a \le -1°C \end{cases}$ $P_{snow} = \quad P - P_{rain}$	(10)
Sublimation of the snowpack [29]	$W_e = \frac{E_l}{\rho_w h_s}$	(11)
The maximum water holding capacity of the snow layer [30]	$\begin{cases} C_r = C_{\min} & \gamma_s \ge \rho_e \\ C_r = C_{\min} + (C_{\max} - C_{\min})(\rho_e - \gamma_s)/\rho_e & \gamma_s < \rho_e \end{cases}$	(12)

Table 3
Formula of snowpack compaction and density [17–19].

	Formula
Destructive metamorphism stage [32]	$\left\lvert\frac{1}{\Delta z}\frac{\partial \Delta z}{\partial t}\right\rvert_{metamorphism} = -2.778\times10^{-6}\times c3\times c4\times\exp[-0.04(273.15-T)]$
	$\begin{cases} c3=c4=1 & \text{if}\gamma_i \le 150kg/m^3 \text{and}\gamma_w=0 \\ c3=\exp[-0.046(\gamma_i-150)] & \text{if}\gamma_i>150kg/m^3 \\ c4=2 & \text{if}\gamma_w=0 \end{cases}$ (13)
Gravity compaction stage [32]	$\left\lvert\frac{1}{\Delta z}\frac{\partial \Delta z}{\partial t}\right\rvert_{overburden} = -\frac{P_s}{\eta_0}\exp[-c5(273.15-T_s)-c6\rho_s]$ (14)
Total compaction rate[17–19]	$\left\lvert\frac{1}{\Delta z}\frac{\partial \Delta z}{\partial t}\right\rvert_{all} = \left\lvert\frac{1}{\Delta z}\frac{\partial \Delta z}{\partial t}\right\rvert_{metamorphism} + \left\lvert\frac{1}{\Delta z}\frac{\partial \Delta z}{\partial t}\right\rvert_{overburden}$ (15)
The rate of the snow density change[17–19]	$\frac{d\rho_s}{\rho_s dt} = -\left\lvert\frac{1}{\Delta z}\frac{\partial \Delta z}{\partial t}\right\rvert_{all}$ (16)

Table 4
Formula of boundary condition [17–19].

Boundary condition	Formula
Neumann boundary condition [21]	$\lambda_s^m\frac{\partial T_s(z,t)}{\partial z}\Big\rvert_{z=h} = L_n(t)+H_s(t)+E_l(t)+Q_p(t)$ (17)
Dirichlet boundary condition [21]	$T_s(z=0,t)=T_g(t)$ (18)

bottom control the energy exchange between the snow layer and the external environment.

In the energy balance formula, Neumann boundary condition [21] is used as the boundary condition of the snow surface, as shown in Eq. (17) in Table 4. It is worth noting that the influence of shortwave radiation is ignored in Neumann boundary condition. The snow bottom is directly connected with the soil. In this paper, it is assumed that the temperature of the snow layer at the interface between the snow layer and the soil is equal to the temperature of the soil, as shown in Eq. (18) in Table 4. As explained in Section 2.1, the soil temperature T_g is assumed to be 0℃.

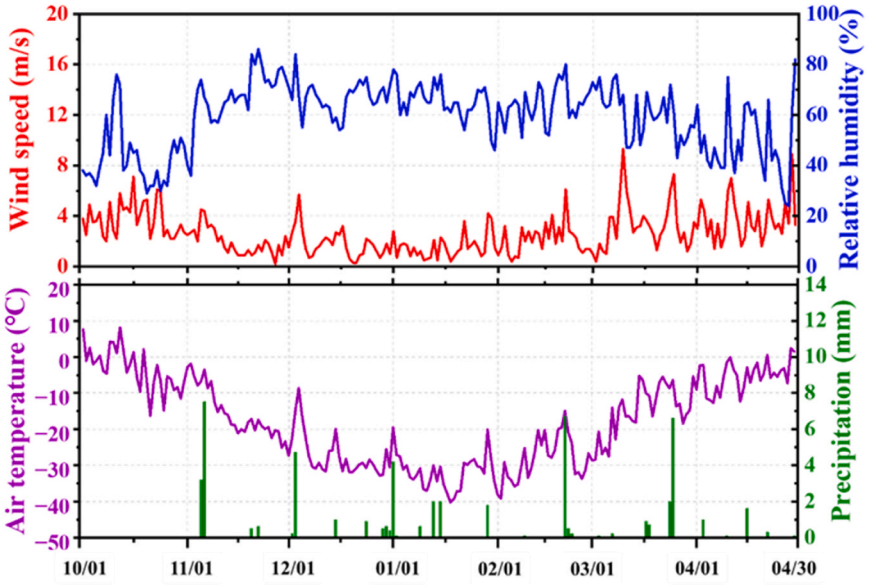

Fig. 3. The meteorological data in the winter of 2005/2006 in Nenjiang.

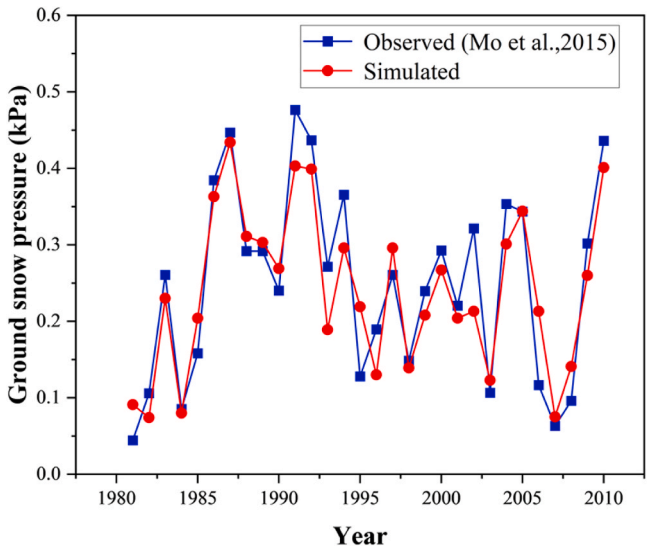

Fig. 4. Comparison between simulated results and observed data of Nenjiang.

In the mass balance formula, the initial boundary conditions are as follows:

$$M(t=0)=0 \tag{19}$$

2.1.5. Snowmelt model validation

Nenjiang, Heilongjiang Province, China, is taken as a case study. Using meteorological data from Nenjiang (Fig. 3 displays the meteorological data for the winter of 2005/2006), the snowmelt model described in the previous section was applied to simulate hourly ground snow pressure over a winter period (from October 1 to April 30 of the following year).

To verify the accuracy of the snowmelt model, the simulation results were compared with the annual maximum snow water equivalent for Nenjiang from 1981 to 2010 (provided by Mo et al. [33]). The annual maximum snow water equivalent was then converted into the annual maximum snow pressure, as shown in Fig. 4. The comparison reveals that the simulated annual maximum ground snow pressure generally follows the observed trend, with only minor deviations. The reasons for these deviations may include the following: maximum snow densities could have occurred due to heavy rainfall and refreezing before observation; minimum snow densities may have been recorded immediately after heavy snowfall, before the snow had undergone sufficient compaction; and meteorological data may have been recorded on earlier days, when instrument accuracy or observation methods were limited, leading to potential errors. This comparison provides evidence of the snowmelt model's accuracy in simulating ground snow pressure.

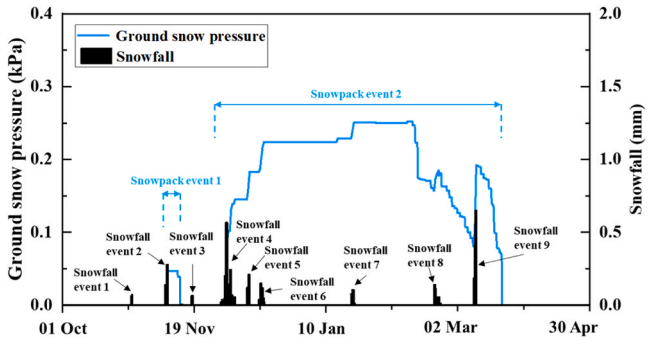

Fig. 5. Snowfall, ground snow pressure in the winter of 2015/2016 in Harbin.

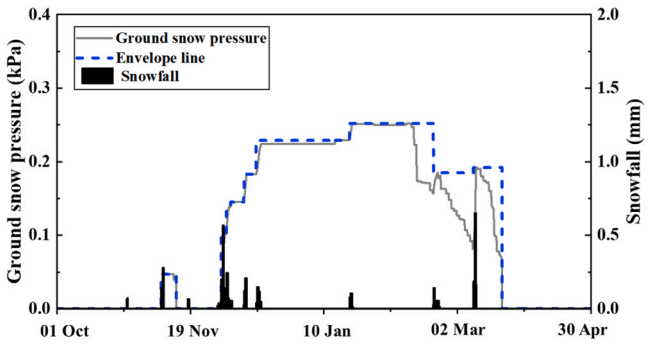

Fig. 6. The envelope line of ground snow pressure.

2.2. Extraction of data pairs

Fig. 5 shows the snowfall and the ground snow pressure calculated by the snowmelt model in Harbin, Heilongjiang Province, China in the winter of 2015–2016 (October 1, 2015 to April 30, 2016). In this paper, a set of continuous snowfall data is defined as a snowfall event, and the process from the beginning of snow accumulation to the end of snow melting is defined as a snowpack event, as shown in Fig. 5. Snow accumulation and melting may occur between two adjacent snowfall events (that is, from the beginning of the previous snowfall event to the end of the next snowfall event), or snow accumulation may not occur due to the small amount of snowfall and high melting rate. To ensure that the snow pressure samples in the subsequent four types of data pairs represent the most unfavorable conditions, the snowpack event can be represented using an envelope line: the snow pressure in each hour between two adjacent snowfall events are modelled as a single cluster having constant intensity equal to the maximum snow pressure. Thus, the envelope line of ground snow pressure can be derived, as shown by the blue dashed line in Fig. 6.

After clustering the ground snow pressure using the method described above, the four methods shown in Fig. 7 can be employed to obtain data pairs. First, the different time periods are divided based on snowfall and snowpack events, and the maximum ground snow pressure within each time period can be obtained. Then, the maximum wind speed within the corresponding time period is identified. The specific methods are as follows:

MethodI: The maximum ground snow pressure between two adjacent snowfall events and the maximum wind speed between two adjacent snowfall events in each snowpack event.

MethodII: Since the snow will not be affected by the wind after three days of precipitation [34], the maximum wind speed within three days after a snowfall and the maximum ground snow pressure between the snowfall event and the next snowfall event are taken.

Method III: The maximum ground snow pressure of a snowpack event and the maximum wind speed within the snowpack event.

Method IV: The maximum ground snow pressure and the maximum wind speed in the whole winter.

2.3. Joint hazard contours

When two highly correlated hazards$V$and$S$act on the building structure simultaneously and their intensity exceeds their respective thresholds v and s, the joint exceedance probability can be expressed as:

$$P(V>v,S>s)=1-F(v)-F(s)+F(v,s) \tag{20}$$

Where $F(v)$ and $F(s)$ respectively represent the best probability model of two hazards, and $F(v,s)$ is the joint probability of the two hazards.

At this point, the joint return period of the two hazards is:

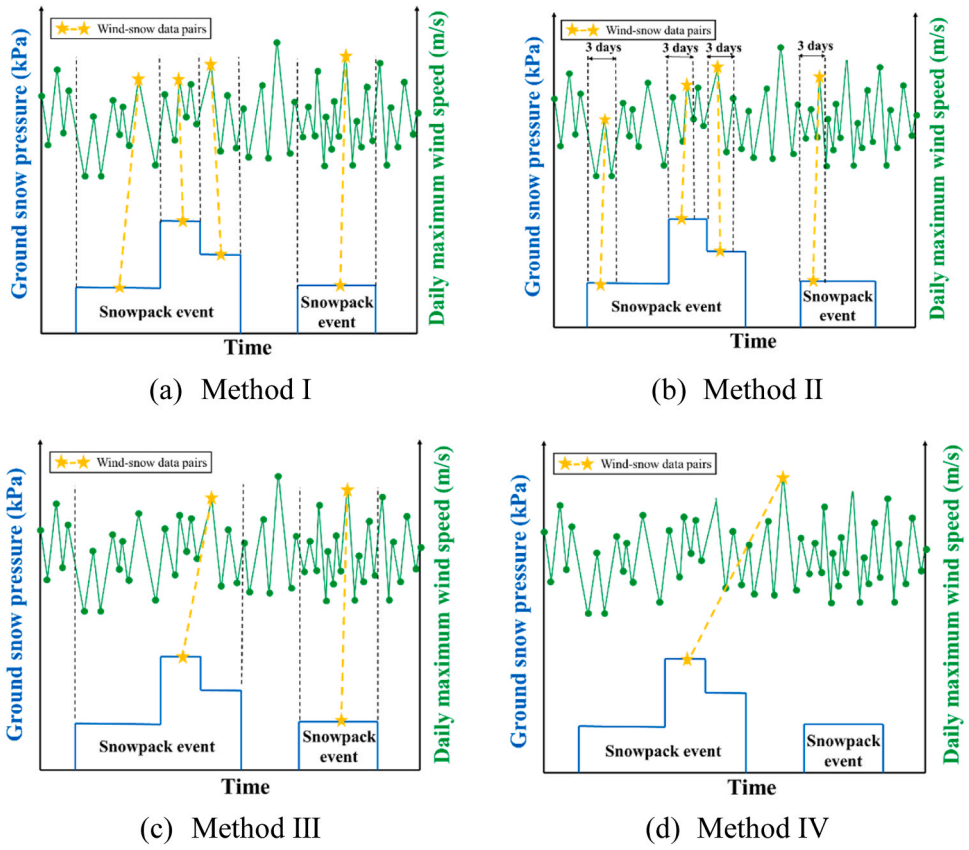

Fig. 7. Methods for getting data pairs of ground snow pressure and wind speed.

$$T = \frac{1}{1 - F(v) - F(s) + F(v,s)} \tag{21}$$

If the correlation between the two hazards is weak or none, the joint exceedance probability distribution of the two hazards can be expressed as:

$$P(V > v, S > s) = 1 - F(v) - F(s) + F(v)\cdot F(s) = (1 - F(v))\cdot(1 - F(s)) \tag{22}$$

At this point, the joint return period of the two hazards is:

$$T = \frac{1}{(1 - F(v))\cdot(1 - F(s))} \tag{23}$$

Therefore, according to Eqs. (21) or (23), based on the best probability model of the two hazards and the selected joint return period, all combination values of hazards of the return period can be calculated. The line formed by these combined values is the joint hazard contour of this return period.

2.4. Combination factor calculation

In addition to the dead loads acting on the structures, various variable loads typically influence the structures as well. However, the probability of multiple variable loads reaching their maximum values simultaneously over the structure's lifetime is very low. Therefore, during the design of the structure, the reduction in the combination of variable loads should be considered. If the maximum value of each variable load during the design reference period is used, the design will be overly conservative and not reflect real conditions. Consequently, we have the following relationship:

$$\sum_{i=1}^{n} S_{i,T} > S_m \tag{24}$$

Where $S_{i,T}$ is T-year load effect of each variable load; S_m is the maximum value of the combined load effect.

In order to make both sides of Inequality (24) equal, the left side of the inequality is multiplied by a factor less than 1:

$$\psi \sum_{i=1}^{n} S_{i,T} = S_m \tag{25}$$

If the load considered is static and has a linear relationship with load effect, the combination of load effects and load combination are basically the same issue. Therefore, ψ in Eq. (26) is the load combination factor:

$$\psi = \frac{S_m}{\sum_{i=1}^{n} S_{i,T}} \tag{26}$$

3. Statistical analysis and Joint wind-snow hazard contours

In this section, the data pairs in 40 representative cities across the country are obtained by the methods described in Section 2. Then the probability models are used to fit the wind speed and ground snow pressure samples in four types of data pairs of each city respectively, after which the best probability model of the two is determined by K-S test and AIC so as to obtain the joint wind-snow hazard contours of different return periods.

3.1. Data pairs of wind speed and ground snow pressure

The meteorological data in this paper are from the website of the China Meteorological Administration (http://data.cma.cn/), including precipitation, temperature, daily temperature difference, wind speed and relative humidity, which are recorded on a daily basis. Among them,

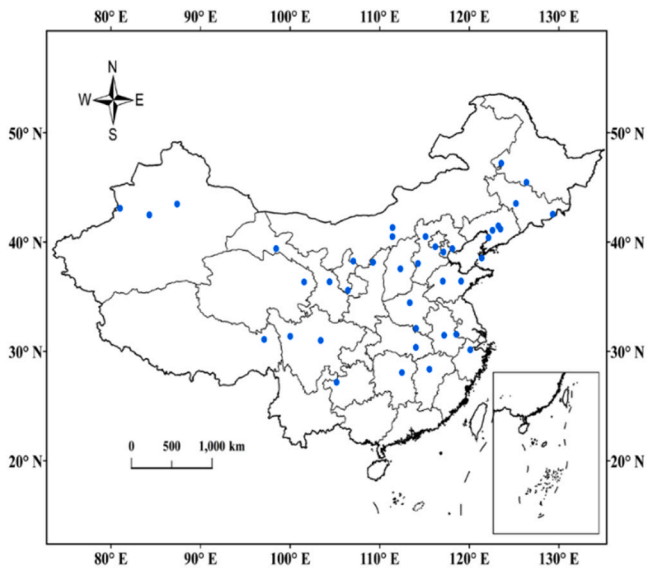

Fig. 8. China map and locations of the 40 representative cities.

the daily maximum wind speed required in this paper is quoted directly from the website, and the ground snow pressure is calculated by the snowmelt model described in Section 2.1. However, the time step of meteorological data used in the calculation of the snow melting process is usually set to 1 h [18]. Therefore, according to the method adopted by Zhou et al [18], the daily meteorological data can be converted into hourly meteorological data. It is assumed that the average relative humidity and average wind speed of each hour in a day are equal to the daily average. The precipitation per hour is the average of the accumulated observed precipitation in 12 h. The hourly average temperature is obtained by linear interpolation between the minimum temperature and the maximum temperature of the day. By this method the hourly meteorological data in over 40 years of 40 representative cities shown in Fig. 8 are calculated. See Appendix A for details. Based on the meteorological data of each city, the hourly ground snow pressure of the 40 cities in each winter can be calculated through the snowmelt model.

Finally, based on the wind speed data and ground snow pressure data of the 40 cities, the data pairs of the 40 cities are obtained by using the four methods described in Section 2.2, which provides a data basis for subsequent research work.

3.2. Fitting probability model

The probability model includes two aspects: the probability distribution function and the corresponding parameter estimation method. The Chinese load code [1] recommends the type-I extreme value distribution (Gumbel) as the best probability distribution of the annual maximum ground snow pressure and the annual maximum wind speed. It also advises using the method of moment (MOM) to estimate the parameters. For comparison, this paper uses the three most common probability distribution functions to fit the wind speed and ground snow pressure samples obtained in Section 2.2, namely Gumbel, lognormal and generalized extreme value (GEV) distributions. For Gumbel distribution, the maximum likelihood method (MLE), moment method (MOM) and least square method (LSM) are used to estimate the parameters respectively. For lognormal distribution, the moment method and maximum likelihood method are used to estimate the parameters

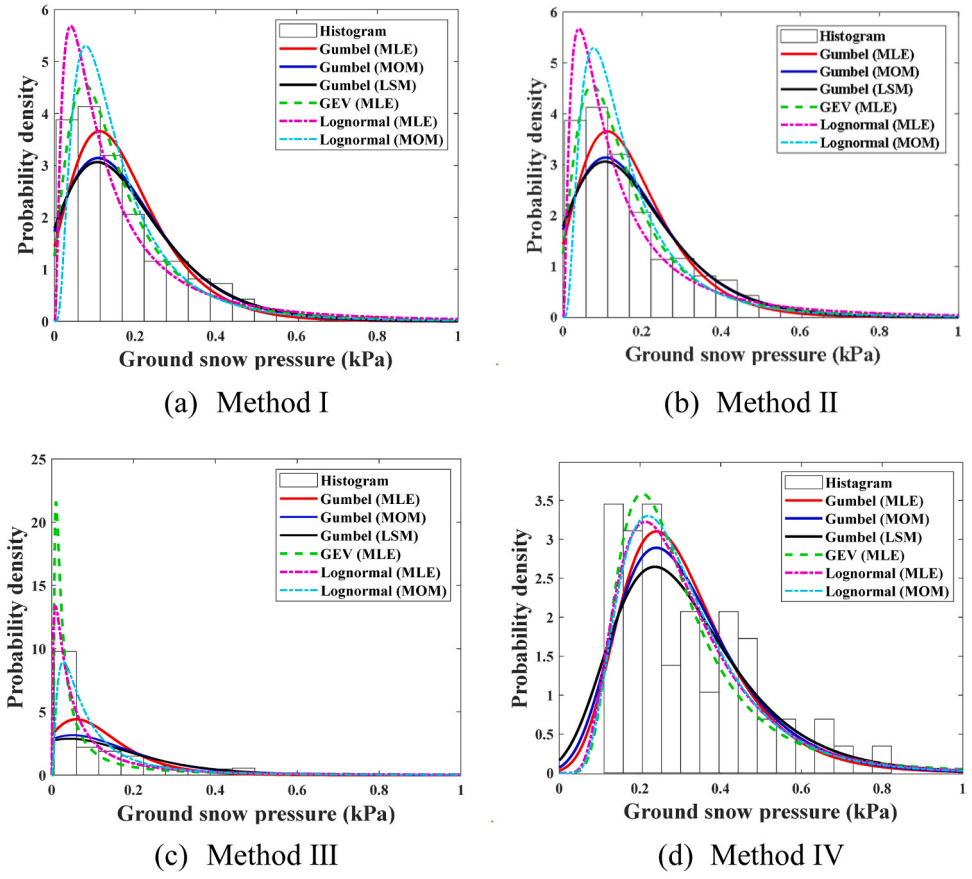

Fig. 9. Comparison of the density histograms of ground snow pressure data in Urumqi and probability density using Gumbel (MLE, MOM, LSM), GEV (MLE), Lognormal (MLE, MOM).

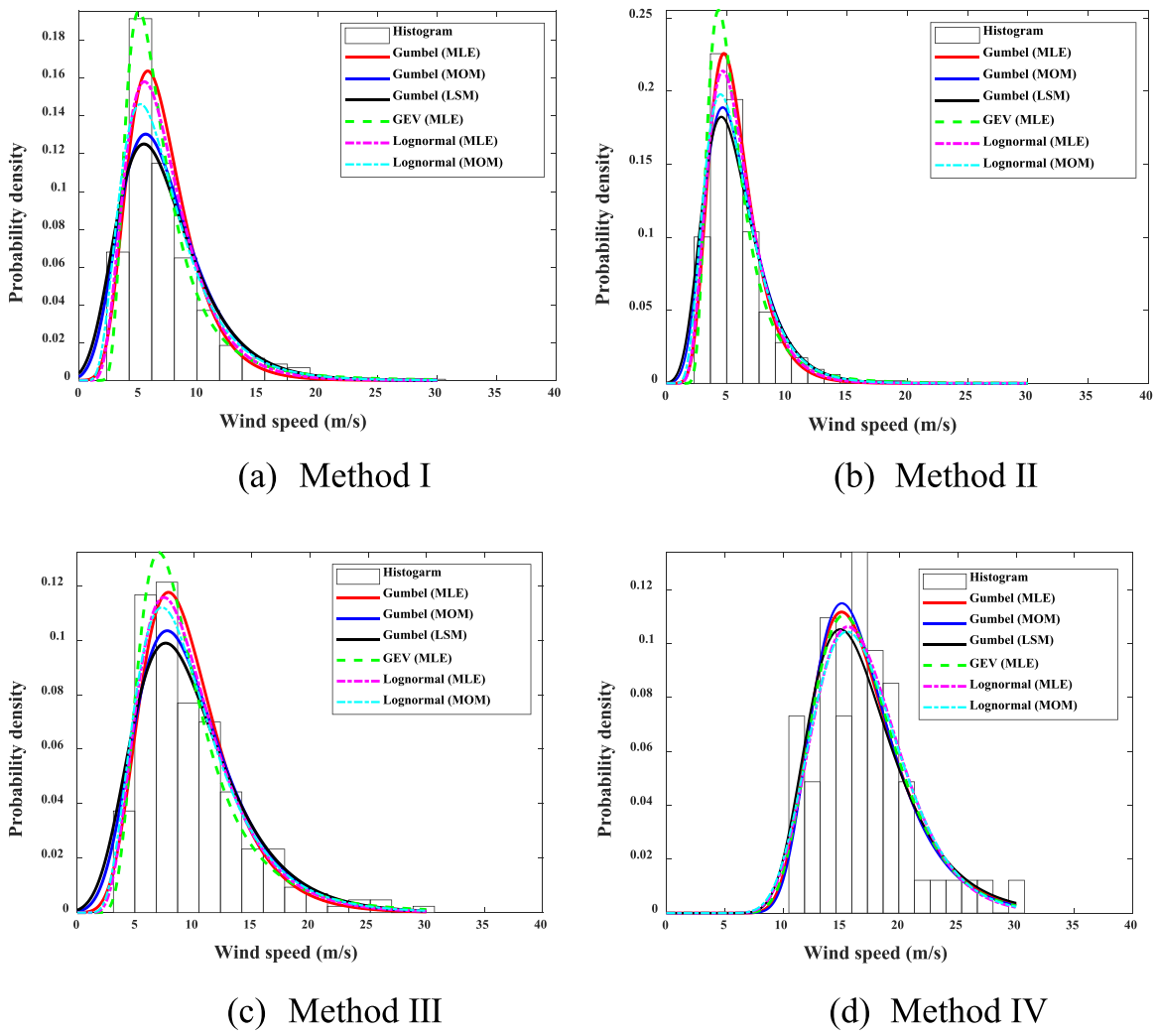

Fig. 10. Comparison of the density histograms of wind speed data in Urumqi and probability density using Gumbel (MLE, MOM, LSM), GEV (MLE), Lognormal (MLE, MOM).

respectively. For the generalized extreme value distribution, the maximum likelihood method is adopted to estimate the parameters. Taking Urumqi as an example, the above probability model is used to fit the ground snow pressure and wind speed in the four types of data pairs of the city, and the results are shown in Fig. 9 and Fig. 10 respectively.

3.3. Goodness-of-fit tests

The goodness-of-fit test determines whether the selected probability model in Section 3.1 can be used to describe wind speed samples and ground snow pressure samples. The most commonly used method is the Kolmogorov-Smirnov test (K-S test) [18, 35, 36], which establishes statistics$D_n$based on the empirical distribution$F_n(x)$and theoretical distribution$F(x)$of the samples:

$$D_n = \max|F(x) - F_n(x)| \tag{27}$$

At a certain significance level θ, for the sample size N, Massey [35] gave the critical value K_θ that the above statistics $D_n$cannot exceed. In general, the significance level is $\theta = 0.05$. When the sample size $N > 35$, $K_\theta = 1.36/\sqrt{N}$. If $D_n > K_\theta$, the sample does not obey the distribution $F(x)$ at the significance level θ. On the contrary, the sample obeys the distribution$F(x)$ at the significance levelθ. The K-S test results of the wind speed and ground snow pressure from four kinds of data pairs in 40 locations are shown in Fig. 11 and Fig. 12. It can be seen that in terms of the wind speed, all probability models perform well across four kinds of data pairs, with GEV (MLE) showing the best performance. However, for ground snow pressure, GEV (MLE) and Lognormal (MLE) work properly at more than 98 % of all locations.

K-S test can only judge whether the alternative probability model is appropriate. However, it cannot determine the best model when multiple probability models pass the test [18,19,36]. Therefore, the Akaike Information Criterion (AIC) proposed by Akaike [37] is adopted here, which quantitatively compares the advantages and disadvantages of each model. Based on the residuals squares sum (RSS), the AIC index calculation formula is defined as follows:

$$RSS = \sum_{i=1}^{N} (x_i - \widetilde{x}_i)^2 \tag{28}$$

$$AIC = N\ln(RSS) + 2k \tag{29}$$

Where k is the number of probability distribution parameters, GEV distribution $k = 3$, Gumbel distribution and lognormal distribution $k = 2$; x_i is the sample value, $\widetilde{x}_i$ is the value with the same non-exceeding probability as x_i estimated by $F(x)$, $\widetilde{x}_i = F^{-1}[F_n(x_i)]$.

The term containing RSS indicates the accuracy of the probability distribution in sample fitting. Apparently, the smaller the RSS, the better the probability model. The number of parameters k indicates the complexity of the probability model, and the smaller the number, the simpler the model. Therefore, the model with the smallest number of parameters and RSS has the smallest AIC. The smaller the AIC, the better

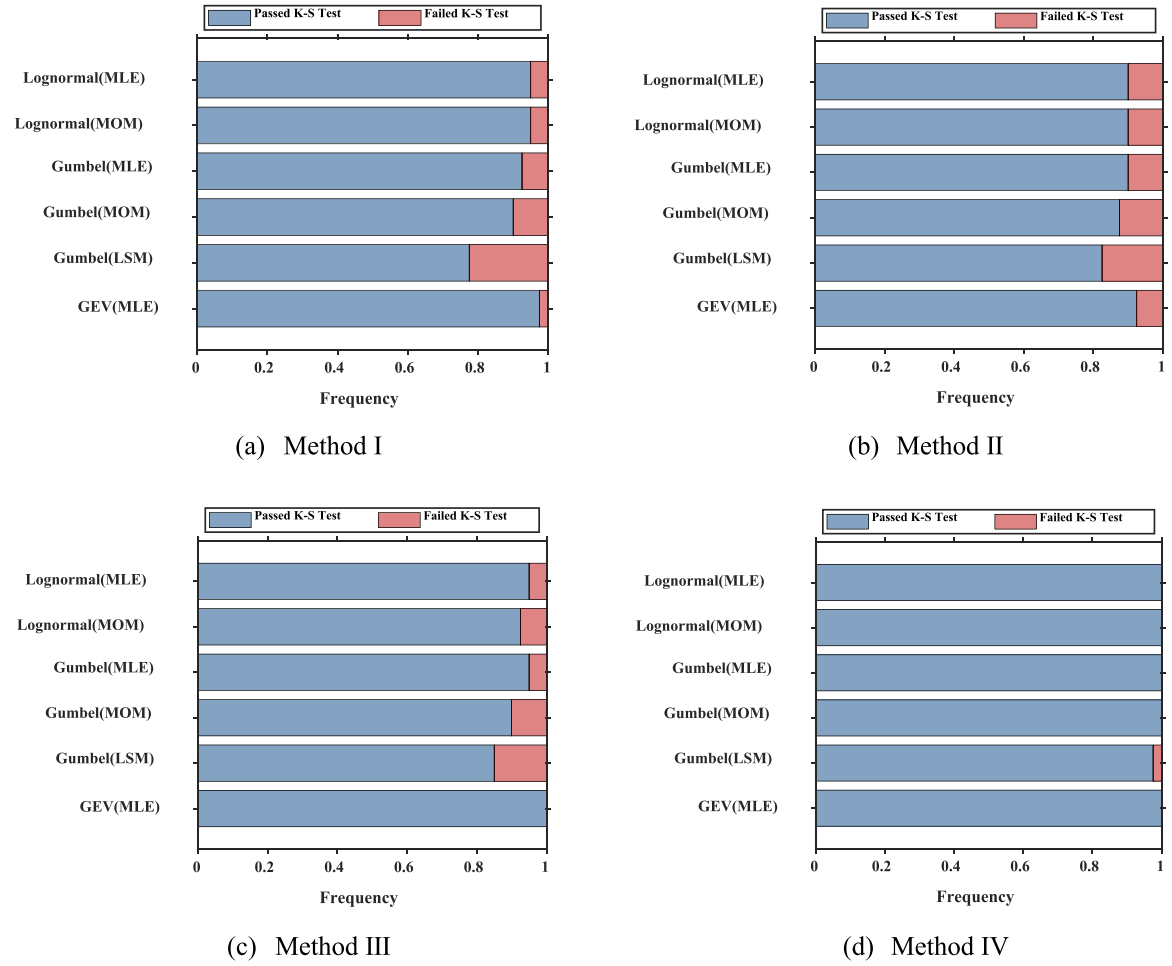

Fig. 11. Pass rate of probability model of wind speed by K-S test.

the model. The probability models for each region, as indicated by AIC, and their corresponding occurrence frequencies are shown in Fig. 13. For wind speed across the four types of data pairs, GEV (MLE) exhibits the highest goodness of fit, followed by Gumbel (LSM). For ground snow pressure, Lognormal (MLE) provides the best fit in the data pairs obtained using methods I, II, and III. However, for the ground snow pressure samples in the data pairs obtained using method IV, GEV (MLE) shows the best fit.

In conclusion, based on the K-S test and AIC comparison, it can be observed that, in the data pairs obtained using methods I, II, and III, the ground snow pressure samples follow the Lognormal (MLE) model. In contrast, the ground snow pressure samples in the data pairs obtained using method IV are better represented by the GEV (MLE) model. For wind speed samples, regardless of the data pairs acquisition method, GEV (MLE) is the probability model with the best goodness of fit. The results are summarized in Table 5.

3.4. Joint wind-snow hazard contours

This paper adopts the linear regression method to analyse the correlation between wind speed samples and ground snow pressure samples. Fig. 14 shows the correlation between wind speed samples and ground snow pressure samples in different data pairs in Urumqi by using the linear regression method. The coefficients of determination R^2 in Fig. 14 are smaller than 0.24, which reflects the very low correlation between the two [38]. The R^2 between wind speed samples and ground snow pressure samples of 40 representative cities is calculated, and the results are shown in Appendix A. It is evident that all R^2 are smaller than 0.24, and the vast majority are below 0.08. Therefore, it can be considered that no matter which type of data pair is concerned, it proves the wind speed samples and ground snow pressure samples are not correlated, that is, they are independent of each other [38]. Therefore, according to Eq. (23), by using the obtained best probability model of wind speed, the best ground snow pressure probability model and the selected joint return period, all combination values of wind speed and ground snow pressure of this joint return period can be calculated. The line formed by these combination values is the joint hazard contour of wind speed and ground snow pressure for the selected return period, namely the joint wind-snow hazard contour. Taking Urumqi as an example, the joint wind-snow hazard contours for the joint return periods of 10 years, 25 years, 50 years, and 100 years are calculated based on four types of data pair, as shown in Fig. 15. From the graph, it can be seen that those contours vary in shapes, which is a result of the different optimal probability models of wind speed samples and ground snow pressure samples in different types of data pair.

4. Study of cases

4.1. Computational model

The research object of this paper is a row of single-axis PV tracker with a length of 100 m, a chord length of 2.4 m, a height of 1.5 m and an inclination of 30 °. Fig. 16 shows its finite element model. It can be seen from the figure that the PV support is composed of a rotating shaft (main beam) and 13 steel columns with the spacing of each column being 8 m. It is worth noting that the top of the column in the middle is equipped

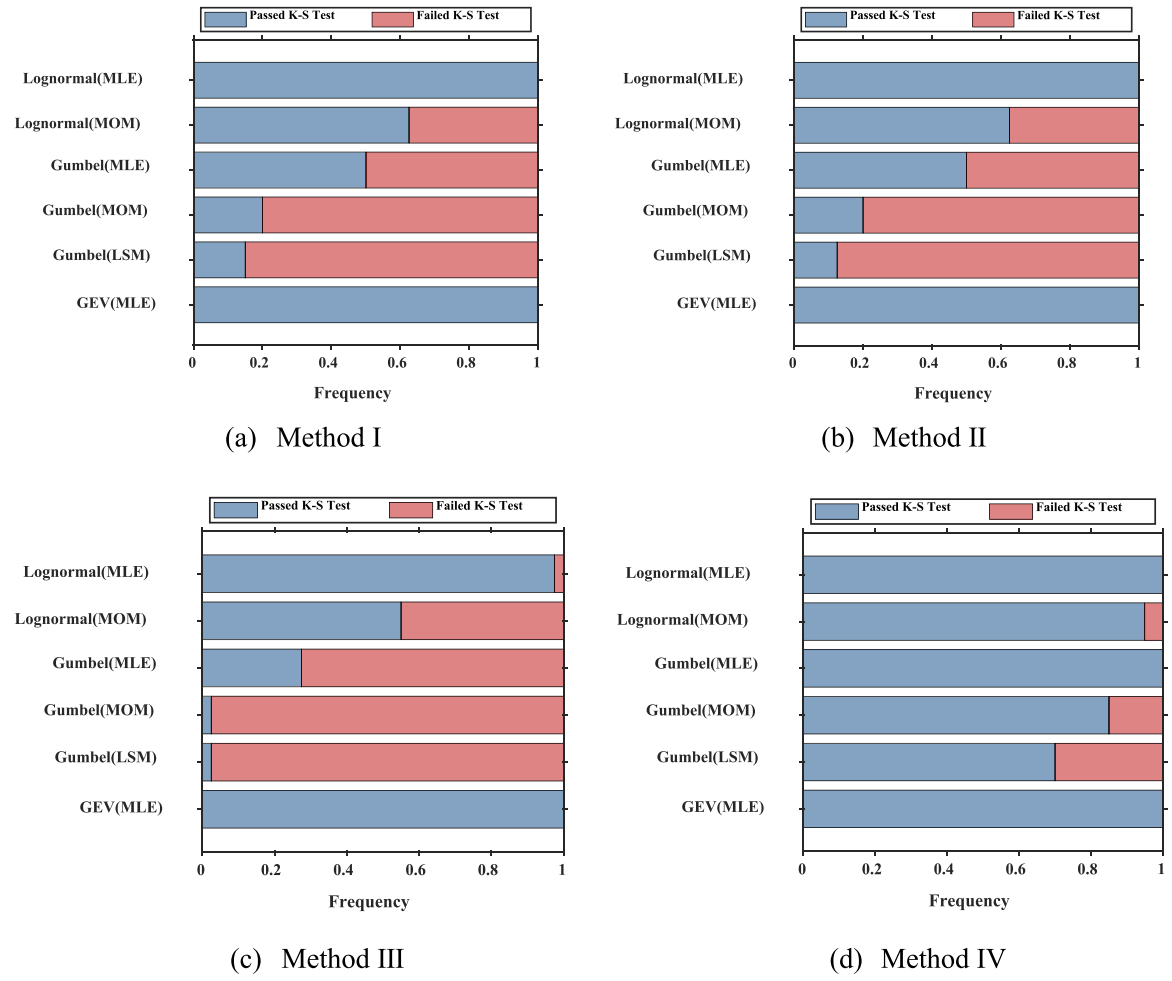

Fig. 12. Pass rate of probability model of ground snow pressure by K-S test.

with a motor that controls the rotation of the PV panel. Thus, it can be taken as a rigid connection with the main beam. For the rest of the columns, their connections with the main beam are regarded as semi-hinged.

4.2. Load combination and load cases

In Section 3.4, the combination values of wind speed and ground snow pressure on the joint wind-snow hazard contours for different return periods are calculated. Subsequently, the wind speed is converted into the characteristic value of wind load, as shown in Table 6. It is important to note that β_z represents the wind vibration coefficient, which is typically taken as 1.2 according to the general code for engineering structures [39]. μ_z is the exposure factor for wind pressure. Assuming terrain roughness is classified as type B, and since the height of the PV tracker is less than 10 m, the value is taken as 1 [1]. μ_s is the shape factor of wind load. Since the shape factor of the wind load of the PV tracker is not given in the code [1], this study refers to the value of open single-slope roofs, as shown in Appendix B. With a 30° inclination angle and under pressure conditions, the shape factors at both ends of the PV panel are μ_{s1}= +1.4, μ_{s2}= +0.6. For uplift forces, μ_{s3}= -1.4, μ_{s4}= -0.6. Other values are calculated by linear interpolation method. The above shape factors correspond to the resultant pressure on the upper and lower surfaces of the PV panel. From this, it can be seen that the wind load follows a trapezoidal distribution along the width of the PV panel [40,41], as shown in Fig. 17. Trapezoidal wind load will impose torque on the main beam. Therefore, the effect of trapezoidal wind load on PV panels can be regarded as the superposition of a uniformly distributed load effect and a torque, as shown in Fig. 17.

In addition, it is worth noting that the transmitted radiation energy is significantly reduced when the panel is fully covered by snow [46]. As a result, the energy yield efficiency of the PV panel is low, leading to minimal heat output from the PV panel. Therefore, the impact of heat transfer between the PV panel and the snowpack is negligible. As mentioned in Section 2.1.1, the ground flux is also minimal. Thus, the characteristic value of the snow load on the horizontal projection plane of the PV panel can be calculated based on the ground snow pressure, as shown in Table 6. μ_r is the snow distribution factor, which is taken as 0.85 based on the reference value of 30°single slope roofs in the code [1]. Since the influence of wind-induced snow drifting is not considered here, the snow load on the PV panel is assumed to be uniformly distributed.

The snow load can only act on the PV panel in the form of pressure, but the wind load can be either a pressure or an uplift force. Therefore, this paper considers the impact of two different combinations of wind and snow loads on the PV support, as shown in Fig. 18. The wind load and snow load in Case I are both pressures. In Case II, the wind load is an uplift force, and the snow load is a pressure.

4.3. Load effect analysis

According to the code for the design of PV support structure [42], the service life of PV support is 25 years. Therefore, the designed reference period should be 25 years. This section uses Urumqi of Xinjiang Province in China as an example, in which the joint wind-snow hazard contour for the 25-year return period calculated by using four different data pairs is

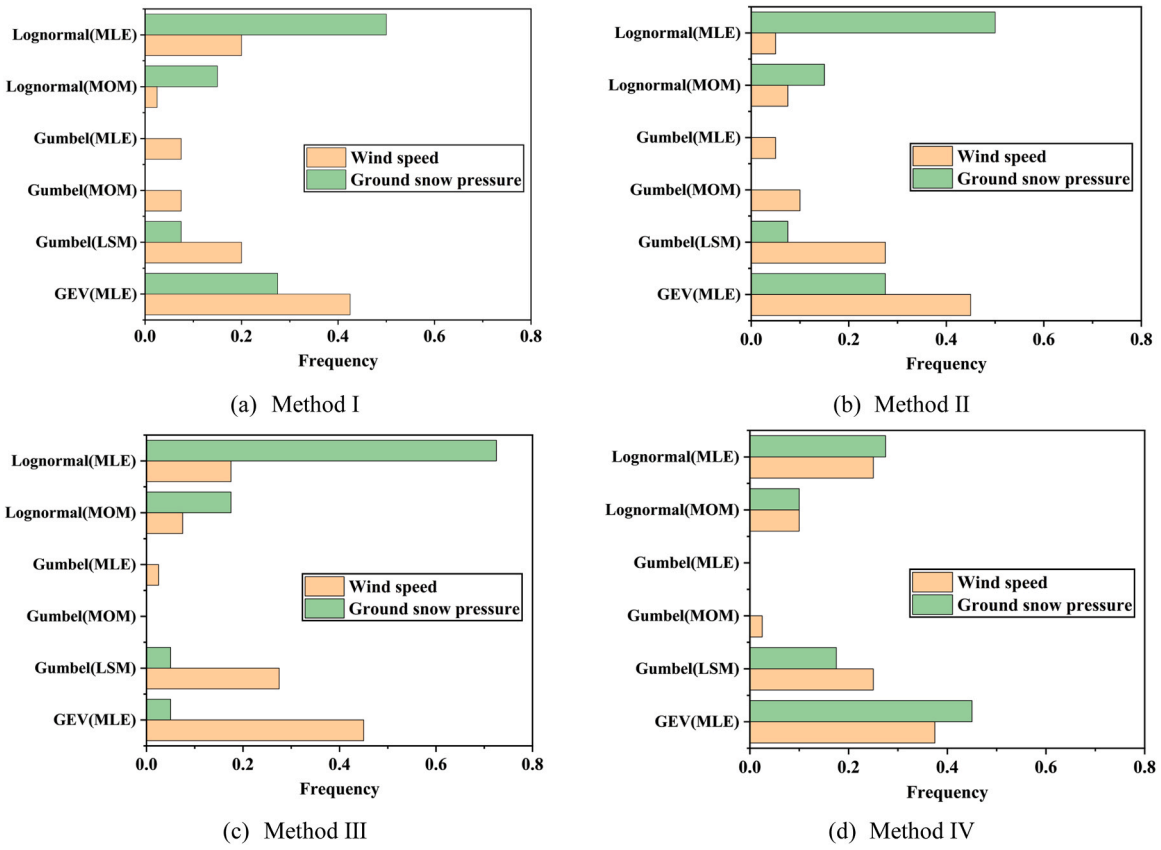

Fig. 13. Goodness-of-Fit of probability model determined by AIC.

Table 5
The best probability model after probability statistics.

Variable	Distribution for different wind-snow data pairs			
	Method I	Method II	Method III	Method IV
Ground snow pressure	Lognormal (MLE)	Lognormal (MLE)	Lognormal (MLE)	GEV (MLE)
Wind speed	GEV (MLE)	GEV (MLE)	GEV (MLE)	GEV (MLE)

selected, as shown in Fig. 19. A series of combination values of wind speed and ground snow pressure on the contour are taken and converted into characteristic values of wind load and snow load according to the method described in the previous section. It is worth noting that the two ends of each joint wind-snow hazard contour in Fig. 19 (i.e., the wind speed when the ground snow pressure is 0 and ground snow pressure when the wind speed is 0) are the wind speed and ground snow pressure for a return period of 25 years, which can be converted into the 25-year characteristic value of wind load w_{25} and snow load s_{25}, as shown in Table 7. Table 7 shows that the w_{25} derived from different data pairs varies significantly, which is due to the different lengths of time for obtaining each maximum wind speed sample by different methods (see Section 2.2 for specific methods). The longer it takes, the larger the sample of maximum wind speed may be obtained, leading to a larger w_{25}. Conversely, w_{25} would be smaller. According to the two cases shown in Fig. 18, the characteristic values of wind and snow loads are loaded on the finite element model of the PV panel shown in Fig. 16, and the three load effects of the PV support are calculated: the maximum axial force of columns P_{max}, the maximum bending moment of main beam M_{max} and the maximum torque of main beam T_{max}.

When the combination mode of Case I is adopted, the wind load is a pressure, and the variation of load effect is shown in Fig. 20. Fig. 20 (a), (b), (c) and (d) show the variation of P_{max} with the combination value of wind speed and ground snow pressure. At this time, the wind load and snow load are both pressures, thus the axial force of the column is negative. In order to visualize the changing trend, the projection of scattered points in space is drawn in the X-Z plane and Y-Z plane. Then $S_{P,m}$, the maximum value of P_{max}, is spotted, as shown by the blue ball in the figure. See Table 8 for specific values. The axial force $S_{P,w_{25}}$ and $S_{P,s_{25}}$ of the column under the action of w_{25} and s_{25} can also be obtained from the graph. See Table 8 for the specific values. Fig. 20 (e), (f), (g) and (h) show the variation of M_{max} corresponding with the combination value of wind speed and ground snow pressure. Then the maximum value $S_{M,m}$ of M_{max} and the bending moments $S_{M,w_{25}}$ and $S_{M,s_{25}}$ of the main beam under the independent action of w_{25} and s_{25} are calculated. See Table 9 for specific values. As the snow load is uniformly distributed, no torque occurs on the main beam, and the torque of the main beam is only related to the wind speed. As shown in Fig. 20 (i), (j), (k) and (l), the maximum torque T_{max} of the main beam increases with the wind speed rising. Therefore, if the combination mode of wind and snow loads in Case I is adopted in the design of PV support and the load effect considered is the axial force of columns and bending moment of the main beam, the combined effect of wind and snow loads should be considered.

It is worth noting that in Fig. 20 (a), (b) and (e), (f) on the 25-year joint wind-snow hazard contour derived from the data pairs obtained by method I and method II, when the wind speed in the combination value of wind speed and ground snow pressure increases and the ground snow pressure almost remains unchanged, the absolute value of the maximum axial force of columns $|P_{max}|$ and the absolute value of the maximum bending moment of main beam $|M_{max}|$ slowly increase and reach the maximum value; when the wind speed further increases and the ground snow pressure decreases, $|P_{max}|$ and $|M_{max}|$ begin to decrease.

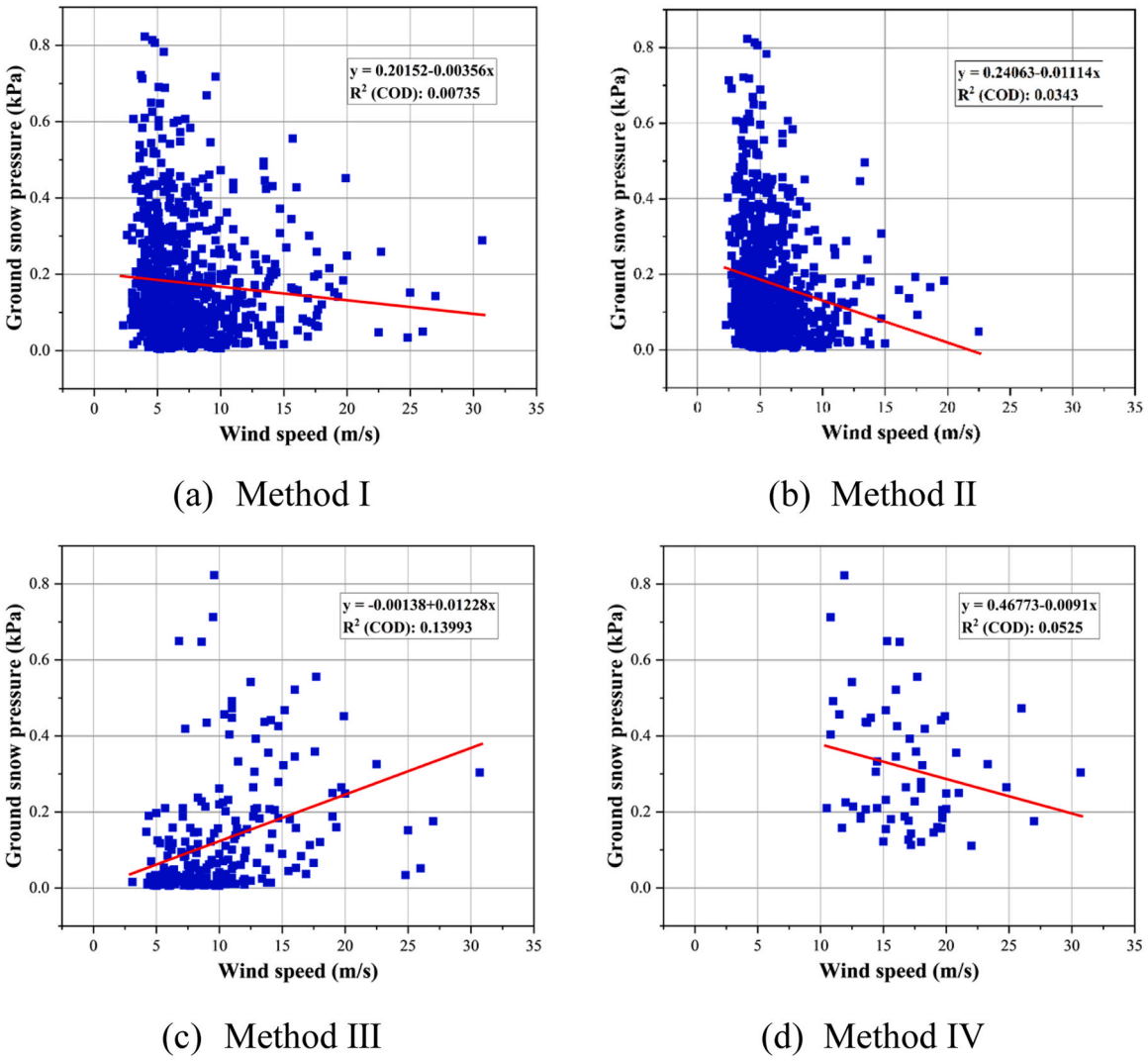

Fig. 14. Correlation between wind speed and ground snow pressure in Urumqi.

Through the comparison of Table 8 and Table 9, it is found that the maximum value of the maximum axial force of columns $S_{P,m}$ and the maximum bending moment of the main beam $S_{M,m}$ under the combined action of wind and snow loads are close to the maximum axial force of columns $S_{P,s_{25}}$ and the maximum bending moment of main beam $S_{M,s_{25}}$ caused by the single action of snow load of the 25-year return period, respectively. This phenomenon proves that the load effect is mainly controlled by snow load at this time. In Fig. 20 (c) and (g), when the wind speed in the combination value of wind speed and ground snow pressure increases and the ground snow pressure almost remains unchanged, the results are similar to those in Fig. 20 (a), (b) and (e), (f), and $|P_{\max}|$ and $|M_{\max}|$ slowly increase and reach the maximum value; when the wind speed further increases and the ground snow pressure decreases, $|P_{\max}|$ and $|M_{\max}|$ begin to decrease. When the wind speed increases to 14 m/s and the ground snow pressure decreases to 0.1kPa, $|P_{\max}|$ and $|M_{\max}|$ start to increase. Through the comparison of Table 8 and Table 9, it is found that $S_{P,m}$ and $S_{M,m}$are close to $S_{P,s_{25}}$ and $S_{M,s_{25}}$ respectively. This phenomenon shows that the load effect is mainly affected by snow load at this time. However, when the wind load increases to 14 m/s, the load effect is mainly controlled by the wind load. In Fig. 20 (d) and (h), unlike the phenomena in the above figures, on the 25-year joint wind-snow hazard contour calculated based on the data obtained by method IV, when the wind speed and ground snow pressure in the combination value of wind speed and ground snow pressure increase and the ground snow pressure almost remains unchanged, $|P_{\max}|$ and $|M_{\max}|$ increase but do not reach the maximum value; when the wind speed further increases and the ground snow pressure decreases, $|P_{\max}|$ and $|M_{\max}|$ increase and slowly reach the maximum value, and the maximum value occurs when the wind speed is 23 m/s and the ground snow pressure is 0.25kpa. Through the comparison of Table 8 and Table 9, it is found that $S_{P,m}$ is close to $S_{P,w_{25}}$ and $S_{P,s_{25}}$, and $S_{M,m}$ is close to $S_{M,w_{25}}$ and $S_{M,s_{25}}$. This indicates that the load effect is controlled by both wind load and snow load.

When the combination mode of Case II is adopted, the wind load is an uplift force. Due to the opposite direction of wind load and snow load, the load effects offset each other. At this point, it can be considered that the load effect caused by wind load is beneficial to the bearing capacity of PV support compared with the load effect caused by snow load, or the load effect caused by snow load is beneficial to the bearing capacity of PV support compared with the load effect caused by wind load. Therefore, if the combination of Case II is adopted in the design of PV support, there is no need to consider the combined effects of wind and snow loads.

4.4. Combination factor of wind and snow loads

As the wind load and snow load considered in this paper are static loads which have a linear relationship with the load effect, the combi-

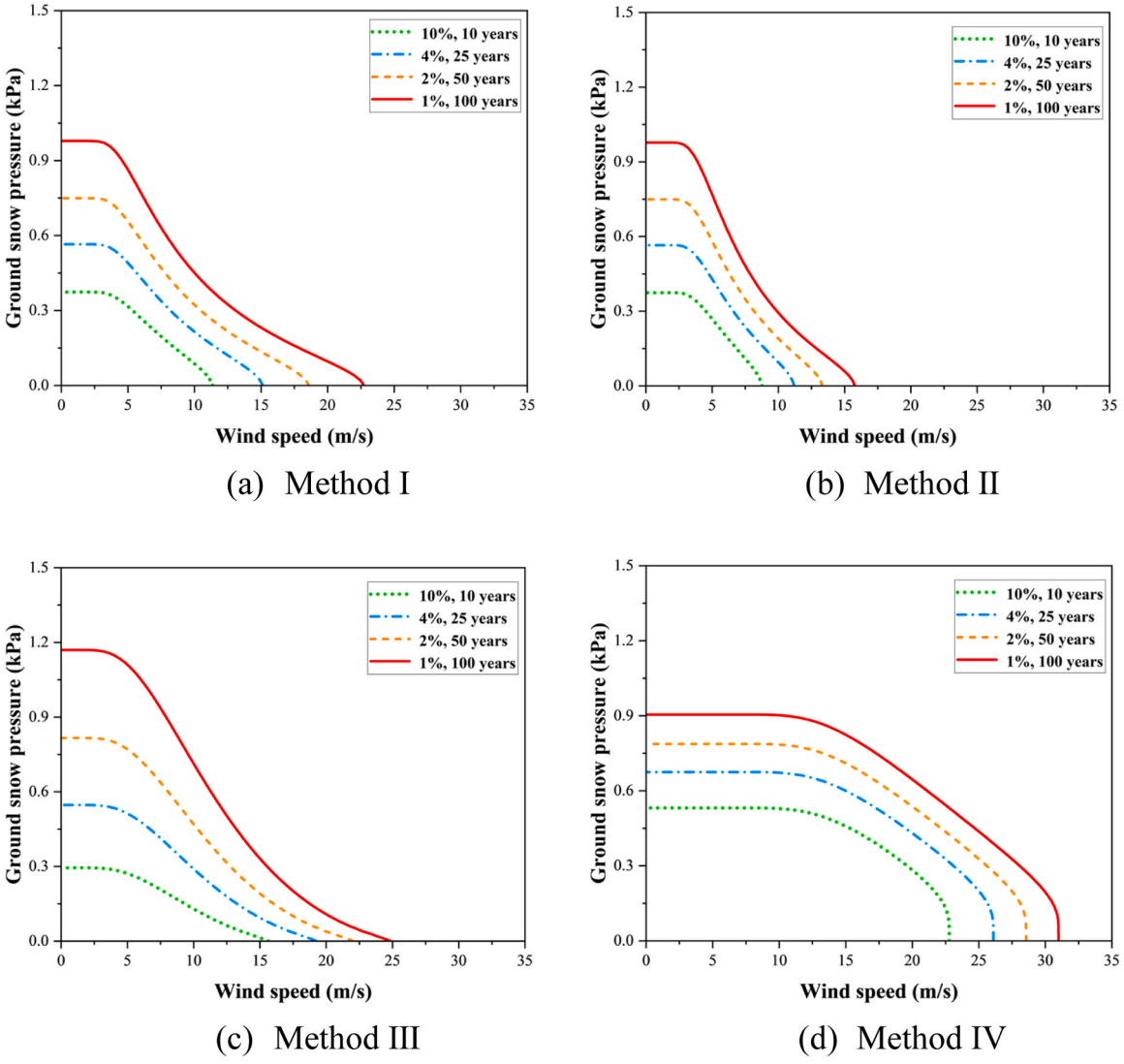

Fig. 15. Hazard level contours for different return periods in Urumqi.

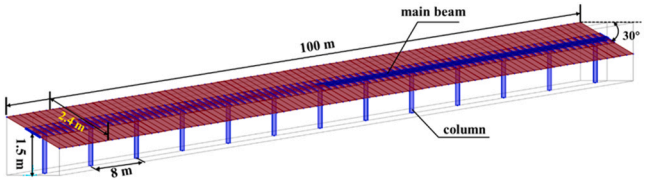

Fig. 16. Computational model of PV panel.

nation factor of wind and snow loads on the PV panel can be calculated according to Eq. (25) in Section 2.4, as shown in the following formula:

$$\psi = \frac{S_m}{S_{w_{25}} + S_{s_{25}}} \tag{28}$$

Where S_m is the maximum value of combined wind and snow load effects, $S_{w_{25}}$ and $S_{s_{25}}$ are the load effects caused by wind load and snow load of the 25-year return period, respectively. It can be seen from Section 5.1 that if the combination mode of wind and snow loads in Case I is adopted in the design of the PV support and the load effect considered in the design process is the axial force of the column and the bending moment of the main beam, the combined effect of wind and snow loads should be taken into consideration. Therefore, $S_{w_{25}}$ is the axial force of columns

Table 6
The formulas of characteristic value of wind and snow loads.

The characteristic value of wind load	$\boldsymbol{w_k = \beta_z \mu_s \mu_z w_0}$ [1]
• The reference wind pressure, w_0	$w_0 = 0.5\rho v_0^2 v_0$ is the reference wind speed (m/s), which is the joint wind-snow hazard contours for different return periods.
• The wind vibration coefficient, β_z	$\beta_z = 1.2$ [39]
• The exposure factor for wind pressure, μ_z	$\mu_z = 1$ [1]
• The shape factor of wind load, μ_s	$\mu_{s1} = +1.4, \mu_{s2} = +0.6$ (pressure) [1] $\mu_{s3} = -1.4$, $\mu_{s4} = -0.6$ (uplift force) [1]
The characteristic value of snow load	$\boldsymbol{s_k = \mu_r s_0}$ [1]
• The reference snow pressure, s_0	s_0 is the ground snow pressure value on the joint wind-snow hazard contours for different return periods.
• The snow distribution factor, μ_r	$\mu_r = 0.85$ [1]

$S_{P,w_{25}}$ and the bending moment of the main beam $S_{M,w_{25}}$ caused by the wind load for the 25-year return period alone, and $S_{s_{25}}$ is the axial force of the column $S_{P,s_{25}}$ and the bending moment of the main beam $S_{M,s_{25}}$ caused by the snow load for the 25-year return period. S_m is the

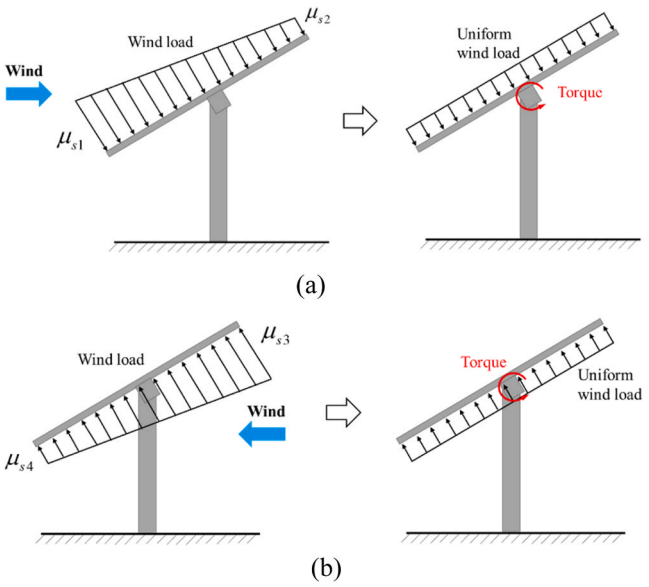

Fig. 17. The decomposed method of wind load on the PV panel.

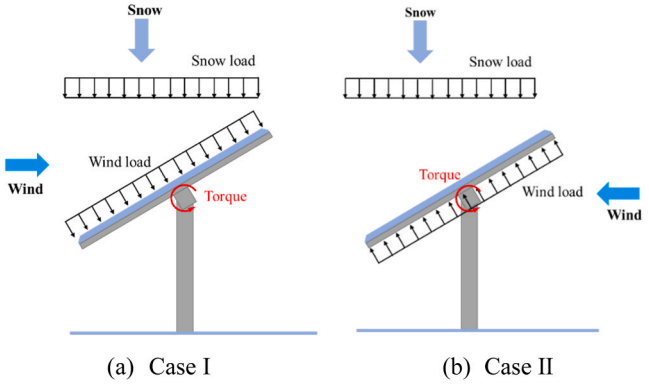

Fig. 18. Wind load and snow load acting on the PV panel.

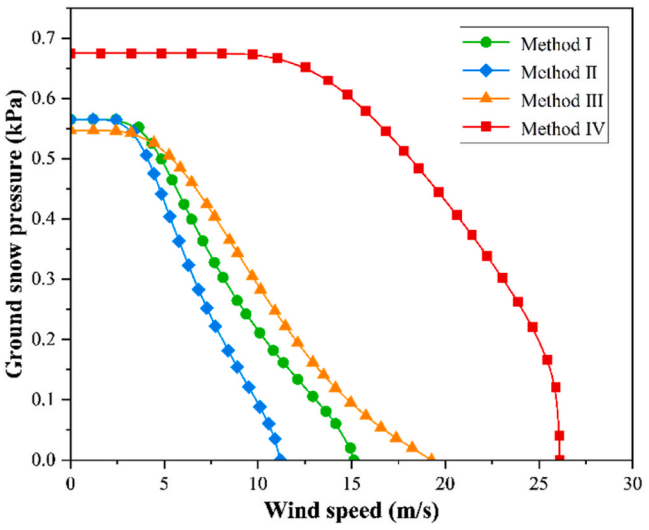

Fig. 19. Hazard level contours for the 25-year return periods in Urumqi.

Table 7
25-year reference wind and snow pressure calculated using data pairs of 4 methods.

Methods	w_{25} (kPa)	s_{25} (kPa)
Method I	0.14	0.57
Method II	0.08	0.57
Method III	0.23	0.55
Method IV	0.43	0.68

maximum value of the maximum axial force of columns ($S_{P,m}$) and the maximum value of the maximum bending moment of the main beam ($S_{M,m}$) under the combined action of wind and snow loads on the 25-year joint wind-snow hazard contour.

Based on the analysis in Section 4.3, the wind and snow load combination factors when considering the axial force of the column and the bending moment of the main beam can be calculated for the design of PV structure in Urumqi. The results are shown in Table 8 and Table 9. Finally, the wind load and snow load on 25-year joint wind-snow hazard contours calculated from four types of data pairs of 40 representative cities are combined in the way of load Case I, and the wind and snow load combination factor of 40 representative cities is calculated, as shown in Appendix C. All results are given in Fig. 21. The top horizontal line of each box chart represents the maximum value, the bottom horizontal line represents the minimum value, and the horizontal line inside the box represents the average value. It can be seen from the figure that if the load effect considered in the design is the axial force of the column, the average value of the wind and snow load combination factors derived from the data pairs obtained by different methods are both 0.68. If the load effect considered is the bending moment of the main beam, the average value of the wind and snow loads combination factors calculated based on the data pairs obtained by different methods are 0.65, 0.65, 0.67 and 0.69, respectively. Therefore, from a comprehensive perspective, when the axial force of columns and the bending moment of the main beam caused by wind and snow loads are considered in the design of PV support, the combination factor of wind and snow loads can be taken as 0.7.

5. Conclusion

This paper takes 40 cities in different regions of China as the research object and uses the multi-layer snowmelt model to simulate the ground snow pressure samples. The data pairs of ground snow pressure and wind speed in winter (referred to as "data pair") is obtained by different methods. The wind speed samples and ground snow pressure samples are fitted by the probability model, based on which the joint wind-snow hazard contour for the 25-year return period is calculated. Finally, the load effect of PV support caused by wind load and snow load is obtained through finite element analysis, and the combination factor of wind and snow loads in each city is calculated. The following conclusions can be drawn from this study:

(1) By comparing the annual maximum ground snow pressure calculated by the multi-layer snowmelt model with the measured data, it can be drawn that the deviation between the two is small and the trend is consistent. The results show that the ground snow pressure can be accurately simulated by inputting the meteorological data into the multi-layer snowmelt model, which provides a solid data basis for this study.
(2) For each city, four methods are used to obtain the data pairs of winter ground snow pressure and wind speed, and six probability models (Gumbel (MLE), Gumbel (MOM), Gumbel (LSM), GEV (MLE), Lognormal (MLE), Lognormal (MOM)) are selected to fit the wind load samples and snow load samples in each data pairs, and then the best probability model is determined by K-S test and AIC. The results show that in the data pairs obtained by methods

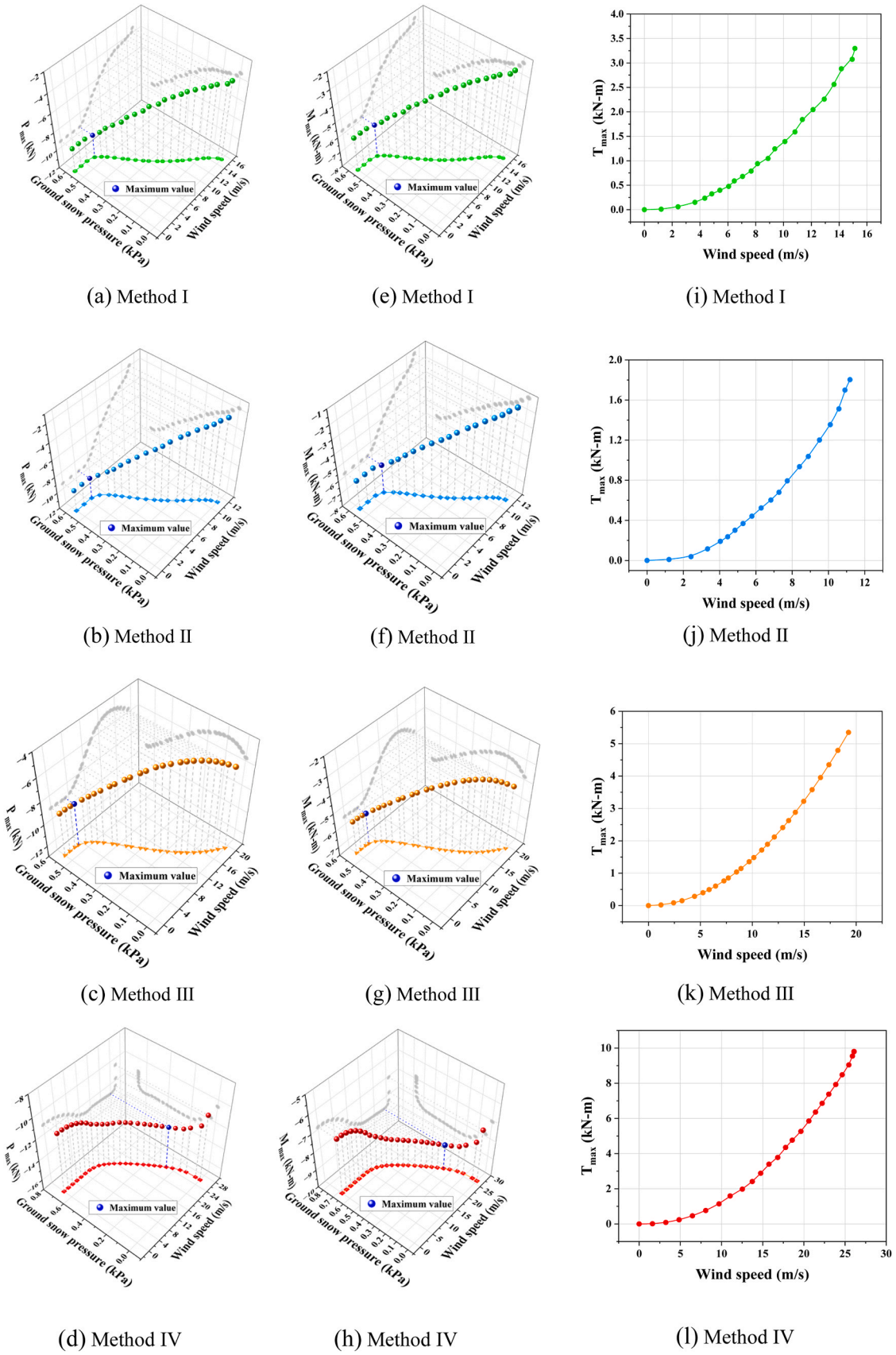

Fig. 20. Variation of maximum axial force of columns ((a), (b), (c), (d)), maximum bending moment of main beam((e), (f), (g), (h)) and maximum torque of main beam ((i), (j), (k), (l)) with data pairs of 4 methods for Case I in Urumqi.

Table 8
Axial force of columns and combination factors: Urumqi as a case.

Methods	$S_{P,w_{25}}$ (kN)	$S_{P,s_{25}}$ (kN)	$S_{P,m}$ (kN)	ψ_P
Method I	−3.56	−9.36	−9.44	0.73
Method II	−1.95	−9.36	−9.42	0.83
Method III	−5.77	−9.05	−9.13	0.62
Method IV	−10.59	−11.18	−12.90	0.59

Table 9
Bending moment of the main beam and combination factors: Urumqi as a case.

Methods	$S_{M,w_{25}}$ (kN-m)	$S_{M,s_{25}}$ (kN-m)	$S_{M,m}$ (kN-m)	ψ_M
Method I	−2.38	−5.76	−5.84	0.72
Method II	−1.30	−5.76	−5.82	0.82
Method III	−3.85	−5.78	−5.65	0.60
Method IV	−7.07	−6.88	−8.60	0.62

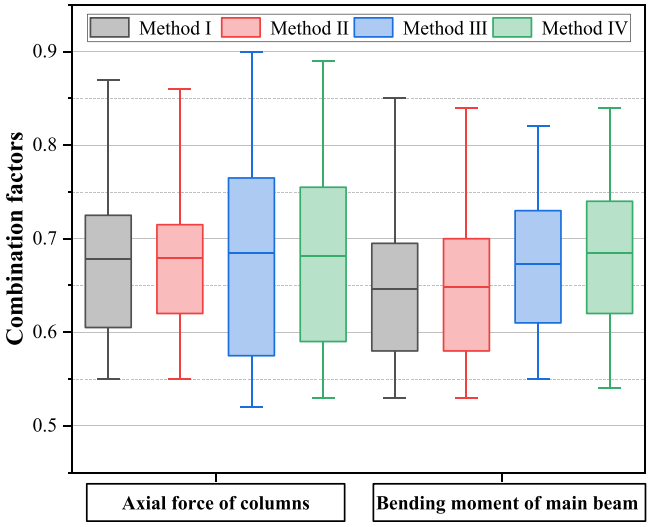

Fig. 21. Combination factors of wind load and snow load for Load Case I in representative cities considering different load effects.

I, II and III of data pairs acquisition, the ground snow pressure samples of more than 50 % of cities follow lognormal (MLE). The ground snow pressure samples in the data pairs obtained by method IV follow GEV (MLE). As for the wind speed samples, GEV (MLE) is the probability model with the highest goodness of fit and the largest number of applicable cities, regardless of the data pairs obtained by either method.

(3) When the wind load and snow load are both pressures, the combination of wind and snow load effects should be considered in the design of PV support. When the wind load is an uplift force and the snow load is a pressure, it is unnecessary to consider the combined effects of wind and snow loads. This is because, at this time, the directions of wind and snow loads are opposite, thus the load effects offset each other. In other words, the load effect caused by the wind is beneficial to the bearing capacity of the PV support compared with the load effect from the snow, or the load effect caused by the snow is better for the bearing capacity of the PV support than that from the wind load. It should be noted that this paper assumes the snow load is uniformly distributed, therefore, it does not consider the uneven distribution of snow load.

(4) When the wind load and snow load are both pressures and the axial force of columns and the bending moment of the main beam are considered in the design of PV support structure, the combination of wind and snow load effects is required, and the combination factor of wind and snow loads is 0.7. If the torque of the main beam is considered, the combination of wind and snow load effects is no longer necessary, as the torque is only caused by the wind load.

6. Limitations and future perspectives

In this study, ground snow pressure is calculated using the multi-layer snowmelt model. The snow load on the PV panel is subsequently determined based on the simulated ground snow pressure. However, the heat transfer between the PV panel and the snowpack is not considered in this analysis. To improve the accuracy of the snow load estimation on the PV panel, the heat flux between PV panel and snowpack can be simulated or measured in the future, and considered in the energy equation of multi-layer snowmelt model.

Wind can also affect the snow load on the PV panel. Specifically, the wind-induced snow drifting can result in the reduction of snow load and the uneven snow distribution on PV panel. Nonetheless, this impact is not considered in this study. To address this, wind tunnel tests and numerical simulations could be conducted to examine the impact of wind-induced snow drifting on the PV panel. Moreover, the snow compaction by wind is also a topic worth studying, which can contribute to further improve the accuracy of the multi-layer snowmelt model.

CRediT authorship contribution statement

Ding Shan: Writing – original draft, Software, Data curation, Conceptualization. **Zhou Xuanyi:** Writing – review & editing, Supervision, Funding acquisition, Conceptualization.

Declaration of Competing Interest

We declare that we do not have any commercial or associative interest that represents a conflict of interest in connection with the work submitted.

Acknowledgments

The authors gratefully acknowledge the support of National Natural Science Foundation of China (Grant numbers 52478546).

Appendix A. . Weather stations selected from Fig. 1

Cities	Latitude	Longitude	Years	Coefficient of determination, R^2			
				Method I	Method II	Method III	Method IV
Harbin	45.45	126.38	1951–2016	0.0022	0.0134	0.0351	0.0140
Qiqihar	47.20	123.56	1951–2016	0.0028	0.0063	0.1749	0.0562
Yanji	42.54	129.31	1953–2016	0.0166	0.0118	0.1484	0.0142
Dalian	38.54	121.38	1951–2016	0.1579	0.1195	0.2314	0.1493

(*continued on next page*)

(*continued*)

Cities	Latitude	Longitude	Years	Coefficient of determination, R^2			
				Method I	Method II	Method III	Method IV
Anshan	41.07	122.59	1951–2016	0.0031	0.0058	0.0076	0.0872
Benxi	41.19	123.47	1955–2016	0.0018	0.0046	0.1105	0.0506
Yingkou	40.40	122.14	1951–2016	0.0204	0.0172	0.2382	0.1078
Shenyang	41.47	123.24	1951–2016	0.0352	0.0237	0.1917	0.0451
Changchun	43.52	125.2	1951–2016	0.0092	0.0179	0.0403	0.1774
Urumqi	43.47	87.37	1951–2016	0.0073	0.0343	0.1399	0.0525
Zhaosu	43.08	81	1954–2016	0.0082	0.0326	0.1380	0.1621
Hohhot	40.49	111.41	1951–2016	0.0039	1.8739e−4	0.0170	0.0158
Siziwang Banner	41.32	111.42	1959–2016	4.4764e−4	6.7647e−5	0.0550	0.0024
Beijing	39.56	116.2	1951–2016	0.0060	0.0181	0.0659	0.0488
Tianjin	39.08	117.11	1951–2016	0.0029	3.2660e−4	0.0590	0.1131
Taiyuan	37.55	112.31	1951–2016	0.0116	0.0169	0.0485	0.0046
Shijiazhuang	41.32	111.42	1951–2016	1.3972e−4	0.0438	0.0089	0.0027
Zhangjiakou	40.50	115.11	1956–2016	0.0026	6.4334e−4	0.0543	0.0019
Tangshan	39.39	118.11	1957–2016	0.0047	0.0019	0.0431	0.0400
Jinan	36.42	117.04	1951–2016	0.0236	0.0209	0.0476	0.0211
Weifang	36.42	119.08	1951–2016	0.0041	0.0014	0.0440	0.0074
Yinchuan	38.25	107.05	1951–2016	0.0598	0.0346	6.5352e−4	0.0057
Guyuan	35.58	106.45	1956–2016	2.1461e−6	0.0064	0.0215	6.0810e−4
Xining	36.35	101.55	1954–2016	4.1983e−4	0.0423	0.0041	2.7386e−5
Jingyuan	36.36	104.39	1951–2016	0.0481	0.0102	0.0460	0.0094
Jiuquan	39.40	98.43	1951–2016	0.0098	0.0185	6.6024e−4	0.0446
Bayanbulak	42.48	84.27	1958–2016	0.0113	0.0203	0.2052	0.0776
Yulin	38.15	109.25	1951–2016	7.6736e−4	0.0016	0.0473	0.0127
Changdu	31.09	97.1	1954–2016	0.0532	0.0102	0.0759	0.0037
Ganzi	31.37	100	1951–2016	5.1315e−4	0.0147	0.0334	0.1397
Hefei	31.47	117.18	1952–2016	1.2359e−4	2.7851e−4	0.0522	3.8154e−4
Hangzhou	30.14	120.1	1951–2016	0.0013	0.0055	0.0712	0.0021
Nanjing	28.36	115.55	1951–2016	0.0527	0.0214	0.0851	0.0427
Zhengzhou	34.45	113.35	1951–2016	0.0078	1.3961e−04	0.0556	0.0181
Xinyang	32.10	114.05	1951–2016	0.0204	7.4810e−5	0.0691	0.0109
Changsha	28.06	112.47	1970–2016	0.0534	0.0605	2.0331e−7	0.0725
Wuhan	30.36	114.03	1951–2016	0.0061	0.0088	0.0504	2.4919e−5
Nanchang	28.36	115.55	1951–2016	0.0018	0.0084	7.7676e−4	0.0011
Dujiangyan	31.00	103.4	1954–2016	0.0052	0.0270	0.1471	0.0484
Bijie	27.18	105.17	1951–2016	6.0445e−4	0.0275	0.0723	0.0641

Appendix B. . The shape factors of open single-slope roof in Chinese load code for the design of building structures (GB 50009—2012) [1]

The shape factors for photovoltaic trackers are not provided in GB 50009—2012 [1]. Therefore, the shape factors for an open single-slope roof can be referenced instead. Specific illustrations and values are shown in Fig. A1 and Table A1, respectively. A comparison with the wind pressure coefficients for photovoltaic trackers based on wind tunnel tests and numerical simulations [11,43] reveals that the shape factors for the open single-slope roof are quite similar.

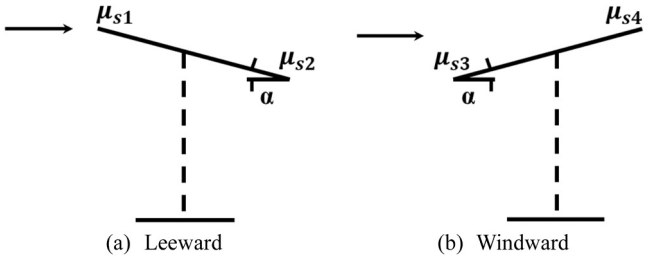

Fig. A1. Schematic diagram of wind direction for the open single-slope roof in GB 50009–2012

Table A1
The shape factors of open single-slope roof in GB 50009—2012 [1]

Inclination angle α (°)	Leeward		Windward	
	μ_{s1}	μ_{s2}	μ_{s3}	μ_{s4}
≤ 10	−1.3	−0.5	+ 1.3	+ 0.5
30	−1.4	−0.6	+ 1.4	+ 0.6

Appendix C. . Combination factors of wind load and snow load for Case I in representative cities considering different load effects

Cities	Load effects							
	Axial force of columns				Bending moment of main beam			
	Method I	Method II	Method III	Method IV	Method I	Method II	Method III	Method IV
Harbin	0.65	0.64	0.70	0.68	0.57	0.56	0.64	0.66
Qiqihar	0.66	0.65	0.70	0.69	0.54	0.53	0.61	0.62
Yanji	0.70	0.70	0.72	0.71	0.60	0.62	0.77	0.79
Dalian	0.55	0.55	0.52	0.54	0.56	0.58	0.56	0.58
Anshan	0.72	0.71	0.75	0.74	0.66	0.65	0.60	0.59
Benxi	0.75	0.74	0.79	0.78	0.71	0.70	0.67	0.67
Yingkou	0.59	0.59	0.62	0.62	0.55	0.55	0.61	0.63
Shenyang	0.69	0.67	0.73	0.72	0.56	0.55	0.55	0.57
Changchun	0.59	0.58	0.67	0.65	0.59	0.61	0.69	0.71
Urumqi	0.73	0.72	0.83	0.82	0.62	0.60	0.59	0.62
Zhaosu	0.67	0.66	0.72	0.70	0.59	0.57	0.58	0.59
Hohhot	0.62	0.64	0.57	0.59	0.57	0.59	0.69	0.71
Siziwang Banner	0.61	0.63	0.54	0.56	0.69	0.70	0.73	0.75
Beijing	0.63	0.65	0.57	0.59	0.63	0.65	0.70	0.72
Tianjin	0.63	0.65	0.57	0.59	0.69	0.70	0.73	0.74
Taiyuan	0.55	0.55	0.64	0.62	0.53	0.53	0.60	0.62
Shijiazhuang	0.71	0.70	0.83	0.82	0.65	0.64	0.70	0.71
Zhangjiakou	0.61	0.62	0.63	0.62	0.58	0.59	0.61	0.63
Tangshan	0.60	0.60	0.66	0.65	0.58	0.58	0.60	0.62
Jinan	0.60	0.59	0.60	0.58	0.54	0.56	0.63	0.65
Weifang	0.59	0.59	0.58	0.57	0.58	0.58	0.63	0.65
Yinchuan	0.77	0.79	0.61	0.63	0.76	0.78	0.82	0.84
Guyuan	0.60	0.62	0.56	0.57	0.58	0.60	0.69	0.71
Xining	0.60	0.62	0.55	0.53	0.63	0.65	0.70	0.72
Jingyuan	0.63	0.65	0.56	0.58	0.64	0.66	0.74	0.75
Jiuquan	0.65	0.67	0.57	0.59	0.66	0.68	0.79	0.81
Bayanbulak	0.55	0.56	0.60	0.58	0.55	0.57	0.68	0.70
Yulin	0.64	0.66	0.55	0.57	0.65	0.67	0.72	0.74
Changdu	0.64	0.64	0.69	0.69	0.60	0.60	0.68	0.69
Ganzi	0.68	0.70	0.63	0.65	0.73	0.74	0.81	0.82
Hefei	0.79	0.78	0.79	0.78	0.70	0.69	0.69	0.69
Hangzhou	0.87	0.86	0.87	0.87	0.81	0.80	0.79	0.79
Nanjing	0.71	0.71	0.71	0.70	0.66	0.66	0.66	0.66
Zhengzhou	0.68	0.67	0.75	0.74	0.61	0.59	0.57	0.59
Xinyang	0.76	0.75	0.78	0.77	0.71	0.70	0.74	0.74
Changsha	0.87	0.86	0.87	0.86	0.82	0.82	0.76	0.75
Wuhan	0.86	0.85	0.85	0.84	0.82	0.81	0.65	0.64
Nanchang	0.70	0.69	0.69	0.67	0.65	0.64	0.55	0.54
Dujiangyan	0.85	0.85	0.90	0.89	0.85	0.84	0.75	0.77
Bijie	0.84	0.83	0.90	0.89	0.82	0.81	0.62	0.61
Mean	**0.68**	**0.68**	**0.68**	**0.68**	**0.65**	**0.65**	**0.67**	**0.69**

Data availability

Data will be made available on request.

References

[1] Ministry of Housing and Urban-Rural Development of the People's Republic of China. Load code for the design of building structures (GB 50009-2012). Beijing: China Architecture & Building Press; 2012.

[2] American Society of Civil Engineers. Minimum design loads and associated criteria for buildings and other structures (ASCE/SEI 7-16). Reston: American Society of Civil Engineers; 2017.

[3] National Research Council Canada. National Building Code of Canada (NBCC 2015). Ottawa: National Research Council of Canada; 2015.

[4] International Organization for Standardization. Bases for design of structures —Determination of snow loads on roofs (ISO 4355-2013). Switzerland: International Organization for Standardization; 2013.

[5] Abiola-Ogedengbe A, Hangan H, Siddiqui K. Experimental investigation of wind effects on a standalone PV (PV) module. Renew Energy 2015;78:657–65. https://doi.org/10.1016/j.renene.2015.01.037.

[6] Reina GP, De Stefano G. Computational evaluation of wind loads on sun-tracking ground-mounted PV panel arrays. J Wind Eng Ind Aerod 2017;170:283–93. https://doi.org/10.1016/j.jweia.2017.09.002.

[7] Chu C, Tsao S. Aerodynamic loading of solar trackers on flat-roofed buildings. J Wind Eng Ind Aerod 2018;175:202–12. https://doi.org/10.1016/j.jweia.2018.02.001.

[8] Ma W, Ma C, Wang C, Han X, Gao F. Wind tunnel experimental study on the wind load interference effect of solar panel arrays. J Exp Fluid Mech 2021;35(4):19–25. https://doi.org/10.1016/j.renene.2022.11.112.

[9] Li S, Mao D, Li S, Wang Q, Yang Q, Chen Y, et al. Wind load characteristics of photovoltaic panel arrays mounted on flat roof. Eng Res Express 2022;4(1). https://doi.org/10.1088/2631-8695/ac57fc.

[10] Ma W, Zhang W, Zhang X, Chen W, Tan Q. Experimental investigations on the wind load interference effects of single-axis solar tracker arrays. Renew Energy 2023;202:566–80. https://doi.org/10.1016/j.renene.2022.11.112.

[11] Xu A, Ma W, Yuan H, Lu L. The effects of row spacing and ground clearance on the wind load of photovoltaic (PV) arrays. Renew Energy 2024;220:119627. https://doi.org/10.1016/j.renene.2023.119627.

[12] Grammou N, Pertermann I, Puthli R. Snow loads on flat roofs with elevated solar panel arrays. Steel Constr 2019;12:364–71. https://doi.org/10.1002/stco.201900031.

[13] Riley D, Burnham L, Snyder W, King B, Dice P. Measurement of Snow Loading on a Tilted PV Module in Northern Michigan. 2022 IEEE 49th Photovoltaics Specialists Conference (PVSC). PA, USA: Philadelphia; 2022. p. 1343–5.

[14] Frimannslund I. Norwegian University of Life Science. Ph.D. dissertation. Resolv snow Chall Increase Deploy Photovolt Syst 2022.

[15] Wang Y, Rosowsky DV. Characterization of joint wind–snow hazard for performance-based design. Struct Saf 2013;43:21–7. https://doi.org/10.1016/j.strusafe.2013.02.004.

[16] Peng Y, Li S, Wang S, Zhao W, Zhou J, Zhou X. Reliability assessment and performance improvement of long-span roof structure subjected to coupled wind-snow multi-hazard. Cold Reg Sci Technol 2023;214:103958. https://doi.org/10.1016/j.coldregions.2023.103958.

[17] Zhou X, Zhang Y, Gu M. Coupling a snowmelt model with a snowdrift model for the study of snow distribution on roofs. J Wind Eng Ind Aerod 2018;182:235–51. https://doi.org/10.1016/j.jweia.2018.09.014.
[18] Zhou X, Xin L, Qiang S. Probabilistic study of snow loads on flat roofs considering the effects of wind at representative sites in China. Struct Saf 2022;99:102242. https://doi.org/10.1016/j.strusafe.2022.102242.
[19] Wu Y, Zhou X, Zhang Y, Gu M. Simulation and statistical analysis of ground snow loads based on a multi-layer snow accumulation and melt model. Struct Saf 2023; 100:102295. https://doi.org/10.1016/j.strusafe.2022.102295.
[20] Zeinivand H, Smedt FD. Prediction of snowmelt floods with a distributed hydrological model using a physical snow mass and energy balance approach. Nat Hazards 2010;54(2):451–68. https://doi.org/10.1016/j.strusafe.2022.102295.
[21] Bartelt P, Lehning M. A physical SNOWPACK model for the Swiss avalanche warning Part I: numerical model. Cold Reg Sci Technol 2002;35(3):123–45. https://doi.org/10.1016/S0165-232X(02)00074-5.
[22] Ohara N, Kavvas M. Field observations and numerical model experiments for the snowmelt process at a field site. Adv Water Resour 2006;29(2):194–211. https://doi.org/10.1016/j.advwatres.2005.03.016.
[23] Walter MT, Brooks ES, McCoo DK, King LG, Molnau M, Boll J. Process based snowmelt modeling: does it require more input data than temperature-index modeling. J Hydrol 2005;300:65–75. https://doi.org/10.1016/j.jhydrol.2004.05.002.
[24] Koivusalo H, Kokkonen T. Snow processes in a forest clearing and in a coniferous forest. J Hydrol 2002;262:145–64. https://doi.org/10.1016/S0022-1694(02)00031-8.
[25] Tarboton DG, Luce CH. Utah energy balance snow accumulation and melt model (UEB). Citeseer; 1996.
[26] Brun E, Martin E, Simon V, Gendre C, Coleou C. An energy and mass model of snow cover suitable for operational avalanche forecasting. J Glaciol 1989;35:333–42. https://doi.org/10.3189/S0022143000009254.
[27] Sun S, Jin J, Xue Y. A simple snow-atmosphere-soil transfer model. J Geophys Res: Atmos 1999;104:19587–97. https://doi.org/10.1029/1999JD900305.
[28] You J. Snow hydrology: the parameterization of subgrid processes within a physical based snow energy and mass balance model, 2004, Utah State University. Ph.D. dissertation.
[29] Dewalle DR, Rango A. Principles of snow hydrology. Cambridge University Press; 2009.
[30] Loth B, Graf HF, Oberhuber JM. Snow-cover model for global climate simulations. J Geophys Res 1993;98(6):451–64. https://doi.org/10.1029/93JD00324.
[31] Anderson E.A. A Point Energy and Mass Balance Model for a Snow Cover. Ph.D. thesis. University of Stanford University; 1976.
[32] Jordan RE. A one-dimensional temperature model for a snow cover: Technical documentation for SNTHERM. Cold Reg Res Eng Lab 1991:89.
[33] Mo H, Fan F, Hong HP. Snow hazard estimation and mapping for a province in northeast China. Nat Hazards 2015;77:543–58. https://doi.org/10.1007/s11069-014-1566-9.
[34] O'Rourke M, DeGaetano A, Tokarczyk JD. Analytical simulation of snow drift loading. J Struct Eng 2005;131(4):660–7. https://doi.org/10.1061/(ASCE)0733-9445(2005)131:4(660).
[35] Massey FJ. The Kolmogorov-Smirnov test for goodness of fit. J Am Stat Assoc 1951; 46(253):68–78. https://doi.org/10.1080/01621459.1951.10500769.
[36] Qiang S, Zhou X, Gu M. Research on reliability of steel roof structures subjected to snow loads at representative sites in China. Cold Reg Sci Technol 2018;150:62–9. https://doi.org/10.1016/j.coldregions.2017.09.005.
[37] Akaike H. A New Look at the Statistical Model Identification. IEEE Trans Autom Control 1998;19:215–22.
[38] Asuero AG, Sayago A, González AG. The Correlation Coefficient: An Overview. Crit Rev Anal Chem 2006;36:41–59. https://doi.org/10.1080/10408340500526766.
[39] Ministry of Housing and Urban-Rural Development of the People's Republic of China. General code for engineering structure (GB 55001-2021). Beijing: China Architecture & Building Press; 2021.
[40] Hsu S, Wu T. Simulated wind action on photovoltaic module by non-uniform dynamic mechanical load and mean extended wind load. Energy Procedia 2017; 130:94–101. https://doi.org/10.1016/j.egypro.2017.09.401.
[41] Hsu S, Lin W, Wu S. Environmental factors for non-uniform dynamic mechanical load test due to wind actions on photovoltaic modules. Energy Procedia 2018;150: 50–7. https://doi.org/10.1016/j.egypro.2018.09.008.
[42] National Energy Administration. Code for Design of Photovoltaic Modules Support Structure (NB/T 10115-2018). Beijing: China planning press; 2018.
[43] Jubayer CM, Hangan H. A numerical approach to the investigation of wind loading on an array of ground mounted solar photovoltaic (PV) panels. J Wind Eng Ind Aerod 2016;153:60–70.
[44] Todd Walter M, Brooks ES, McCool DK. Process-based snowmelt modeling: does it require more input data than temperature-index modeling? J Hydrol 2005;300: 65–75.
[45] Zeinivand H, De Smedt F. Prediction of snowmelt floods with a distributed hydrological model using a physical snow mass and energy balance approach. Nat Hazards 2010;54:451–68.
[46] Perovich DK. Light reflection and transmission by a temperate snow cover. J Glaciol 2007;53:201–10.